

# Computational modeling in clay mineralogy

**AIPEA Educational Series**

**Publication No. 3**

Lectures held mainly at the 3<sup>rd</sup> AIPEA School for Young Scientists  
Instituto Andaluz de Ciencias de la Tierra, Granada, Spain, July, 2017

*Edited by C. Ignacio Sainz-Díaz*

*Series Editor: Saverio Fiore*





# Atomistic modeling of clays and related nanoporous materials with ClayFF force field<sup>†</sup>

**Andrey G. Kalinichev**

Laboratoire SUBATECH (UMR 6457 - Institut Mines-Télécom Atlantique,  
Université de Nantes, CNRS/IN2P3), Nantes, France  
International Laboratory for Supercomputer Atomistic Modelling and Multi-Scale Analysis,  
National Research University Higher School of Economics, Moscow, Russia

*† The paper is based on the material of two invited lectures given by the author at the AIPEA School for Young Scientists “Computational Modeling In Clay Mineralogy”, Granada, Spain, July 2017, and the Workshop “Argilla Studium-2019”, Moscow, Russia, November 2019.*

## 1. Introduction

Clay minerals present a specific challenge for understanding their structure and properties from an atomistic perspective. Typical micron-scale size of clay crystals in combination with the stacking disorder of their individual platelets pose technical limits to our ability to fully evaluate atomic positions and crystal structures of these materials. Unless relatively large and perfectly ordered single crystals are available, standard X-ray diffraction techniques are not usually capable of providing full atomic details of clay minerals. Low crystal symmetry of clays, their greatly diverse chemical compositions, atomic defects and isomorphic substitutions, layer stacking disorder, variable water content and interlayer ionic composition – all these and many other related issues significantly complicate atomic scale characterization and understanding of clays and their aqueous interfaces (e.g., Bergaya *et al.*, 2006). At the same time, the methods of atomistic computational modeling of materials have already become mature enough to serve as a powerful complementary tool for quantitative evaluation of the structure and properties of clays and other clay-related materials.

The methods of computational atomistic modeling of materials had been initially developed in the mid-1950s and for a long time remained a research area for purely theoretical chemical physics and physical chemistry dealing with rather abstract and very simplified models of solids and liquids (Allen and Tildesley, 2017; Frenkel and Smit, 2002). Because of the very limited computational power available at the time, it took almost twenty years before these approaches were first applied to realistic molecular systems, even as simple as water (Berensen *et al.*, 1981, 1987; Kalinichev, 2001). And it took another twenty years of computer hardware and software advances before these methods were started to be cautiously applied for the modeling of complex materials with more realistic atomic structure and composition, important for practical applications, such as clays (Delville, 1991; Skipper *et al.*, 1991, 1995a, 1995b).

However, over the last twenty years the clay-minerals community is gradually appreciating the value of the quantitative insights provided by atomistic computational modeling approaches. These techniques not only help to develop and test crystallographic models of clay structures, but also provide critical insights into understanding the fundamental mechanisms that control many physical and chemical properties of clay minerals and clay-related thermodynamic, kinetic, and reactive processes. Atomistic computer simulations can now help in the detailed quantitative interpretation of the data obtained by various experimental techniques – IR, Raman, NMR, Brillouin spectroscopies, X-ray and neutron diffraction, mass spectrometry, etc. (Ferrage *et al.*, 2011; Kirkpatrick *et al.*, 2015; Marry and Rotenberg, 2015; Kalinichev *et al.*, 2016; Szczerba *et al.*, 2016a,b; Kraevsky *et al.*, 2020). In turn, this new experimental knowledge provides a valuable feedback for building better and more accurate atomistic models of clay-related materials and processes.

To a significant extent, this progress was stimulated by the development of a simple and robust ClayFF force field (Cygan *et al.*, 2004) – a specific set of parameters that empirically describes interatomic interactions within the clay mineral structure and with various molecules and ions at their aqueous or non-aqueous interfaces. This Chapter provides a brief introduction to the theoretical concepts on which the techniques of atomistic computer simulations of materials are based in general, describes the functionality of ClayFF, and then illustrates the application of ClayFF in the atomistic simulations of several clay-related problems.

## 2. Basic approaches to classical atomistic modeling of materials

The so-called classical methods of atomistic simulations can be roughly sub-divided into two groups: deterministic and stochastic. These are, respectively, the methods of molecular dynamics (MD) and Monte Carlo (MC). In both cases the simulations are typically performed for a relatively small number of interacting particles (atoms, ions, and/or molecules;  $1,000 < N < 1,000,000$ ) confined in a box with periodic boundaries also called the simulation cell. An example of such simulation cells for modeling a swelling clay structure and a clay-water interface are schematically shown in Figure 1. Atomistic simulations generate a large number of instantaneous atomic configurations, and this microscopic information on the positions and velocities of all atoms of the simulated system over certain period of time can be directly transformed into many useful thermodynamic, structural, and transport properties of this system with the help of rigorous relationships of statistical mechanics (McQuarrie, 2000; Frenkel and Smit, 2002; Allen and Tildesley, 2017). In most cases, the principal requirement for the validity of the statistical-mechanical formalism is the assurance that our system is in the state of thermodynamic equilibrium in the macroscopic sense, even though in the microscopic sense all atoms in the system are in permanent thermal motion.

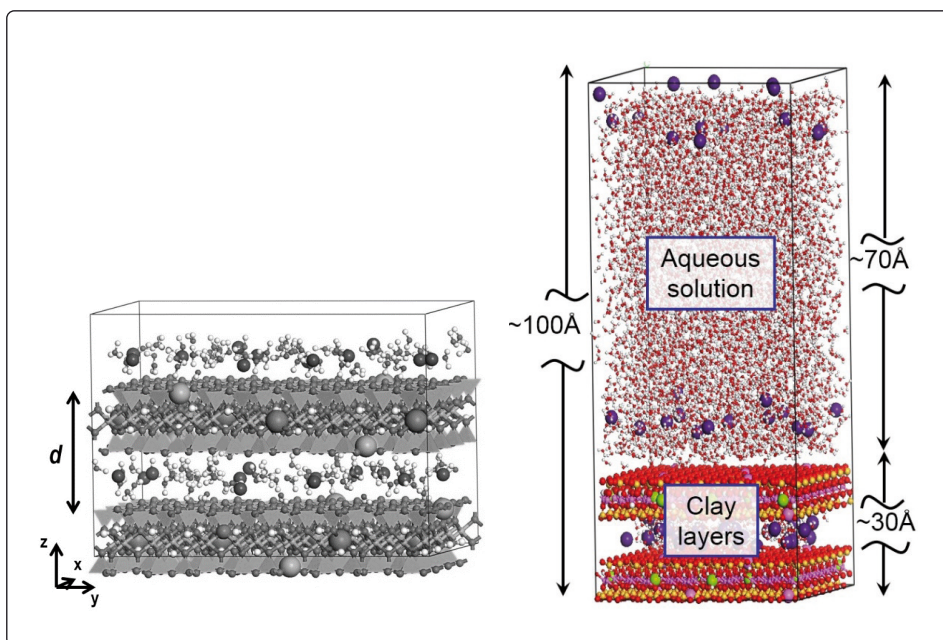


**Figure 1.** Left: A periodic model of a smectite structure. Right: General scheme of a typical simulation cell for atomistic modeling of clay interfaces with aqueous solutions.

## 2.1 Molecular dynamics simulations

In MD simulations, the classical Newtonian equations of motion are numerically integrated for all  $N$  interacting particles in the simulation box. The size of the time step for integration depends on a number of factors, including temperature and density, masses of the particles and the nature of the interparticle potential, and the general numeric stability of the integration algorithm. In the MD simulations of aqueous systems, the time step is typically of the order of femtoseconds ( $10^{-15}$  s), and the dynamic trajectories of the molecules are usually followed (after a thermodynamic pre-equilibration) for  $10^5$  to  $10^7$  steps, depending on the properties of interest and the size of the system.

The resulting knowledge of the dynamic trajectories for each of the particles (i.e. particle positions, velocities, as well as orientations and angular velocities if molecules are involved) means a complete description of the system in a classical mechanical sense. The thermodynamic properties of the system can then be calculated from the corresponding time averages along the equilibrium MD trajectory. For example, the temperature is related to the average value of the kinetic energy of all molecules in the system:

$$T = \frac{2}{3Nk_B} \left\langle \sum_{i=1}^N \frac{m_i \mathbf{v}_i^2}{2} \right\rangle \quad (1)$$

where  $k_B$  is the Boltzmann constant,  $m_i$  and  $\mathbf{v}_i$  are the masses and the velocities of the particles in the system, respectively, and the angular brackets denote the time-averaging along the equilibrium dynamic trajectory of the system.

Pressure can be calculated from the virial theorem (McQuarrie, 2000):

$$P = \frac{Nk_B T}{V} - \left( \frac{1}{3V} \right) \left\langle \sum_{i=1}^N \mathbf{r}_i \cdot \mathbf{F}_i \right\rangle \quad (2)$$

where  $V$  is the volume of the simulation box and  $(\mathbf{r}_i \cdot \mathbf{F}_i)$  means the scalar product of the position and the force vectors of particle  $i$ .

The heat capacity of the system can be calculated from temperature fluctuations:

$$C_V = R \left( \frac{2}{3} - N \frac{\langle T^2 \rangle - \langle T \rangle^2}{\langle T \rangle^2} \right)^{-1} \quad (3)$$

where  $R$  is the gas constant. In the Equations (1)-(3), the angular brackets denote time-averaging along the dynamic trajectory of the system.

Molecular dynamics simulations may be performed under a variety of conditions and constraints, corresponding to different *ensembles* in statistical mechanics. Most commonly the *microcanonical* (*NVE*) ensemble is used, i.e., the number of particles, the volume, and the total energy of the system remain constant during the simulation. The relationships (1)-(3) are valid for this case. There are several modifications of the MD algorithm, allowing one to carry out simulations in the *canonical* (*NVT*) or *isothermal-isobaric* (*NPT*) ensembles. Relationships similar to Equations (1)-(3) and many others can be systematically derived for these ensembles, as well (Frenkel and Smit, 2002; Allen and Tildesley, 2017).

## 2.2 Monte Carlo simulations

In MC simulations, a large number of particle configurations are generated on a computer using a random number generator by the following scheme, assuring that all of them belong to the same thermodynamic equilibrium state of the model system. Starting from a given (almost arbitrary) configuration, a trial move of a randomly chosen particle to a new position is attempted. The potential energy difference,  $\Delta U$ , associated with this move is then calculated, and if  $\Delta U < 0$ , the new configuration is unconditionally accepted. However, if  $\Delta U > 0$ , the new configuration is not automatically rejected. Instead, the Boltzmann factor  $\exp(-\Delta U/k_B T)$  is calculated and compared with a randomly chosen number between 0.0 and 1.0. The new configuration is accepted if the Boltzmann factor is larger than this number, and rejected otherwise. In other words, the trial configuration is accepted with the following probability:

$$p = \begin{cases} 1, & \Delta U \leq 0; \\ \exp\left(\frac{-\Delta U}{k_B T}\right), & \Delta U > 0. \end{cases} \quad (4)$$

Reiteration of such a procedure gives a *Markov chain* of molecular configurations distributed in the phase space of the system, with the probability density proportional to the Boltzmann weight factor corresponding to the canonical *NVT* statistical ensemble (Frenkel and Smit, 2002; Allen and Tildesley, 2017).

Typically, many millions of configurations are generated after some pre-equilibration stage of about the same length. The thermodynamic properties of the system can then be calculated as the averages over the ensemble of configurations. The equivalence of ensemble-averages and time-averages, the so-called *ergodic hypothesis*, constitutes the basis of statistical mechanics (e.g., McQuarrie, 2020).

The advantage of the MC method is that it can be more readily adapted to the cal-

culations of averages in any statistical ensemble (Frenkel and Smit, 2002; Allen and Tildesley, 2017). Thus, to perform simulations in the  $NPT$  ensemble, one can introduce volume-changing moves. All intermolecular distances are then scaled to a new box size. The acceptance criterion is then also changed accordingly. Instead of the energy difference  $\Delta U$  in Equation (4), one should now use the enthalpy difference:

$$\Delta H = \Delta U + P\Delta V - k_B T \ln \left( 1 + \frac{\Delta V}{V} \right)^N \quad (5)$$

where  $P$  is the pressure (which is kept as a constant parameter the same way as temperature) and  $V$  is the volume of the system.

In the  $NPT$  ensemble, besides the trivial averages for configurational (i.e. due to the intermolecular interactions) enthalpy:

$$H_{conf} = \langle U \rangle + P\langle V \rangle \quad (6)$$

and particle density:

$$\rho = \frac{N}{\langle V \rangle} \quad (7)$$

one can easily calculate such useful thermodynamic properties as isobaric heat capacity  $C_p$ , isothermal compressibility  $\kappa$ , and thermal expansivity  $\alpha$  can be easily calculated from the corresponding fluctuation relationships (McQuarrie, 2000; Frenkel and Smit, 2002; Allen and Tildesley, 2017):

$$C_p = \left( \frac{\langle H^2 \rangle - \langle H \rangle^2}{Nk_B T^2} \right) \quad (8)$$

$$\kappa \equiv \frac{1}{V} \left( \frac{\partial V}{\partial P} \right)_T = \left( \frac{\langle V^2 \rangle - \langle V \rangle^2}{Nk_B T \langle V \rangle} \right) \quad (9)$$

$$\alpha \equiv \frac{1}{V} \left( \frac{\partial V}{\partial P} \right)_p = \left( \frac{\langle H_{conf} V \rangle - \langle H_{conf} \rangle \langle V \rangle}{Nk_B T^2 \langle V \rangle} \right) \quad (10)$$

The *grand canonical* ( $\mu VT$ ) statistical ensemble, in which the chemical potential of the particles is fixed and the number of particles may fluctuate, is particularly attrac-

tive for simulations of clay systems where hydration and swelling is usually one of the important processes. Within the MC method, the algorithm of GCMC involves additional random moves to insert or remove particles into our system (e.g., H<sub>2</sub>O molecules in the interlayers of a smectite clay, Ferrage *et al.*, 2011). GCMC method can be directly applied to the calculation of thermodynamic adsorption and swelling isotherms, a challenge for traditional MD methods. However, various versions of the MD simulations in the grand canonical statistical ensemble have also been recently introduced (e.g., Loganathan *et al.*, 2018, 2020).

### 2.3 Periodic boundary conditions

One of the most obvious difficulties of both atomistic simulation methods is the relatively small system size, always much smaller than the Avogadro number,  $N_A$ , characteristic for a truly macroscopic system. Therefore, the simulations are usually performed by applying so-called *periodic boundary conditions* to the simulation box in order to minimize surface effects and to mimic more closely its bulk macroscopic properties. This means that the basic simulation box (see, e.g., Figure 1) is assumed to be surrounded by identical images of the box in all three dimensions infinitely. Thus, if during the simulation a particle leaves the box through one side, its image simultaneously enters the box through the opposite side, because of the identity of the boxes. In this way, the problem of surfaces is circumvented at the expense of introducing a larger scale periodicity to the entire system.

How well the simulated properties of a small infinitely periodic system can represent the properties of a macroscopic system depends on the range of the intermolecular potential and the property under investigation. This is especially important for the interactions involving long-range electrostatic forces (or Coulomb interactions), which is always the case with materials like clays and aqueous salt solutions. Several methods to treat these long-range electrostatic interactions are commonly used (see, e.g., Allen and Tildesley, 2017), of which the *Ewald summation* is usually considered as the most satisfactory one.

With the widespread availability of free and ready-to-use software packages for atomistic simulations, the implementation of a particular statistical ensemble in MC or MD simulations or various algorithms to accurately account for long-range interatomic interactions has become routine even for an end user without deep knowledge of statistical mechanics, such as most of the clay researchers. However, both MC and MD methods rely heavily on the accurate description of the interactions among all atoms of the model system, which are usually represented by a set of interatomic potentials, and it is generally assumed that the total potential energy of the system can be described as a sum of these interactions. In classical molecular simulations, the interaction potentials are often based on empirical fits to available experimen-

tal data for thermodynamic and structural properties of materials or use the results of corresponding quantum chemical calculations (Allen and Tildesley, 2017). The practical success of any set of potential energy functions—referred to collectively as a *force field*—ultimately depends on the quality and accuracy of the energy expression in reproducing experimental chemical structures, physical properties, and spectroscopic observations. There are several successful force fields designed specifically for modeling clay minerals and clay-related environmental processes (Skipper *et al.*, 1995a; Teppen *et al.*, 1997; Smith, 1998; Sainz-Diaz *et al.*, 2001; Cygan *et al.*, 2004; Heinz *et al.*, 2013; Tesson *et al.*, 2018). The following sections describe and discuss the formalism of the ClayFF force field (Cygan *et al.*, 2004), its later modifications (Zeitler *et al.*, 2014; Pouvreau *et al.*, 2017, 2019), and its application to the atomistic modeling of various clay-related materials and processes.

### 3. ClayFF construction and parametrization

The ClayFF parametrization was originally developed in response to a strong need for a robust and flexible force field suitable for atomistic simulations of mineral/water interfaces, most particularly – clays and clay-related phases, including metal (oxy)hydroxides, layered double hydroxides (LDHs), etc. (Cygan *et al.*, 2004). Atomistic computational modeling of such interfaces is especially challenging, because their solid mineral substrate is often incompletely or poorly characterized both in terms of their crystal structure and in terms of their composition. They typically have large unit cells, low crystal symmetry, and greatly variable composition. They also frequently occur as only micron to sub-micron size particles.

Earlier simulations of such systems relied, almost exclusively, on the empirical parametrizations using the basic assumption that all atoms in the clay structure are rigidly fixed to their crystallographic positions (e.g., Skipper *et al.*, 1995a, 1995b; Smith, 1998; Marry *et al.*, 2008; Botan *et al.*, 2013). This posed limitations on the accurate description of all structural and dynamics aspects of interactions between the solid substrate and the interfacial fluid, while still allowing the degrees of freedom associated with swelling and lateral displacement of each individual clay layer as a whole.

There are two principal ways to overcome this limitation and introduce realistically necessary atomic mobility and flexibility of such complex hydrated solid substrates. One can, of course, introduce a set of interaction parameters explicitly describing all covalent bonds in the structure in addition to commonly used so called “non-bonded” terms of the force field accounting for electrostatic and dispersive (van-der-Waals, VDW) interatomic interactions. In this approach, all covalent bonds must be identified and evaluated for each possible local interatomic coordination (e.g., Teppen *et al.*, 1997, Sainz-Díaz *et al.*, 2001; Heinz *et al.*, 2013). However, the application of this approach to systems with complex and often ill-defined bond struc-

tures can be problematic due to the lack of reliable experimental data to constrain all the parameters necessary for a full description of all bonded interactions. For such complex situations, force field parameters must be readily transferable among diverse models and simulations, and it is strongly preferable that the overall functional form of the force field is preserved simple enough to allow modeling of highly disordered systems containing large numbers of particles and to effectively capture their complex and often cooperative behavior.

With this argumentation in mind, the development of ClayFF was based on an alternative approach: to treat the majority of bonded interactions in the crystals as “quasi-ionic” (i.e., formally non-bonded), and require that the proper crystal structures and local atomic coordinations are maintained solely by a careful balance between interatomic electrostatic attractions and VDW repulsion terms of the force field. This greatly simplified approach requires a dramatically smaller number of force field parameters for its implementation, and allows for molecular simulations of even highly disordered and complex systems containing large numbers of atoms.

Thus, the total potential energy in ClayFF is represented as the sum of the contributions from the Coulombic ( $E_{Coul}$ ) and van der Waals ( $E_{VDW}$ ) interactions of all atomic pairs, while the explicit bond stretch and angle bend interaction terms are only preserved for molecular entities, such as H<sub>2</sub>O, polyatomic ions, organic molecules, but also for the OH groups in the clay structure (Cygan *et al.*, 2004; 2009):

$$U = E_{Coul} + E_{VDW} + E_{Bond\ Stretch} + E_{Angle\ Bend} \quad (11)$$

where

$$E_{Coul} = \frac{e^2}{4\pi\epsilon_0} \sum_{i \neq j} \frac{q_i q_j}{r_{ij}} \quad (12)$$

$$E_{VDW} = \sum_{i \neq j} D_{0,ij} \left[ \left( \frac{R_{0,ij}}{r_{ij}} \right)^{12} - 2 \left( \frac{R_{0,ij}}{r_{ij}} \right)^6 \right] \quad (13)$$

In Eq. (12)-(13)  $q_i$  and  $q_j$  are the partial charges on the interacting atoms,  $e$  is the elementary charge, and  $\epsilon_0$  is the dielectric permittivity of vacuum ( $8.85419 \times 10^{-12}$  F/m). The VDW term combines the short-range interatomic repulsions (positive term) as two atoms closely approach each other and the dispersive attraction (negative term) in the functional form of a (12-6) Lennard-Jones potential, where  $D_{0,ij}$  and  $R_{0,ij}$  are empirical parameters derived from the fitting of the model to observed structural and physical property data.  $D_{0,ij}$  and  $R_{0,ij}$ , and the partial atomic charges are the key parameters in ClayFF. The VDW parameters between the unlike atoms

are calculated according to the so-called Lorentz-Berthelot combining rules – the arithmetic mean for the distance parameter,  $R_0$ , and the geometric mean for the energetic parameter,  $D_0$ :

$$R_{0,ij} = \frac{R_{0,i} + R_{0,j}}{2} \quad (14)$$

$$D_{0,ij} = \sqrt{D_{0,i} D_{0,j}} \quad (15)$$

Explicit bonded interactions (the last two terms in Eq.(11)) are only used to describe the O-H bonding in  $\text{H}_2\text{O}$  molecules, structural -O-H groups, and the covalent bonding in polyatomic dissolved species such as sulfate (Kalinichev and Kirkpatrick, 2002), ammonium (Loganathan and Kalinichev, 2013) or uranyl (Teich-McGoldrick *et al.*, 2014). In these cases, the Coulombic and VDW interactions are excluded for the explicitly bonded atoms, while the bond stretching (e.g., -O-H) and bond angle bending (e.g., H-O-H) interactions are simplified to include only harmonic terms:

$$E_{\text{Bond Stretch } ij} = k_1 (r_{ij} - r_o)^2 \quad (16)$$

$$E_{\text{Angle Bend } ijk} = k_2 (\theta_{ijk} - \theta_o)^2 \quad (17)$$

where  $k_1$  and  $k_2$  are the harmonic force constants, and  $r_o, \theta_o$  – equilibrium values of the bond length and bond angle, respectively.

For water molecules, the flexible version of the simple point charge (SPC) potential was originally used (Berendsen *et al.*, 1981, Teleman *et al.*, 1987), although its slightly modified version SPC/E (Berendsen *et al.*, 1987) was also later successfully used (e.g., Ferrage *et al.*, 2011; Holmboe and Bourg, 2014). More complex inharmonic terms can also be used to describe the bond bending and stretching terms in Eq. (11) (e.g., Greathouse *et al.*, 2009; Zeitler *et al.*, 2014; Szczerba *et al.*, 2016a). In all cases, the force field parameters for aqueous cations and anions are largely incorporated from published intermolecular functions compatible with the respective molecular model of  $\text{H}_2\text{O}$ .

Another very important general simplification of the ClayFF parametrization is the assumption that the VDW terms centered on all types of O atoms in crystal structures are the same as those  $O_{\text{H}_2\text{O}}$  of the SPC water oxygens, while those centered on the H atoms of structural O-H groups were ignored (Cygan *et al.*, 2004). However, the charges on the O and H atoms can vary depending on their occurrence in  $\text{H}_2\text{O}$  molecules, hydroxyl groups, and bridging sites.

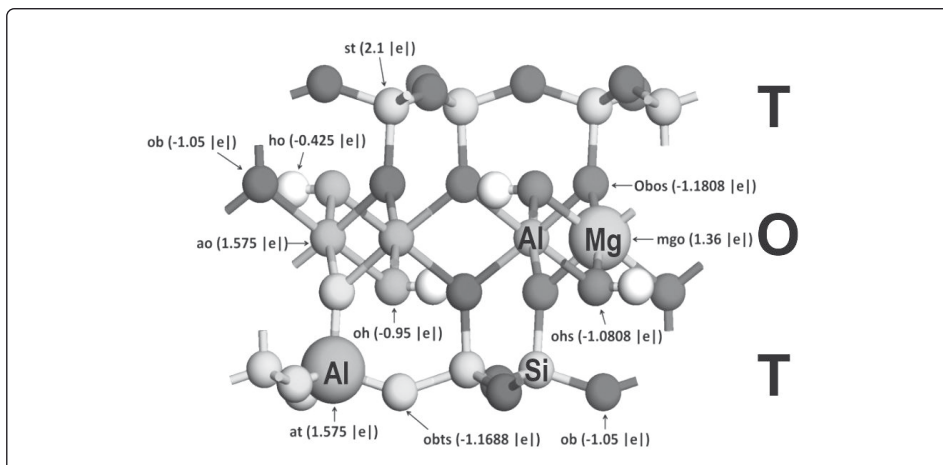


**Figure 2.** Schematic representation of a montmorillonite unit cell fragment with tetrahedral and octahedral substitutions and different atomic charge distributions according to the ClayFF force field (Table 1). ob (bridging oxygen), obts (bridging oxygen with tetrahedral substitution), obos (bridging oxygen with octahedral substitution), oh (hydroxyl oxygen), ohs (hydroxyl oxygen next to octahedral substitution), at (Al in tetrahedral coordination), ao (Al in octahedral coordination), mgo (Mg in octahedral coordination), st (Si in tetrahedral coordination).

The empirical parameters in ClayFF (Table 1) were originally optimized with the objective to accurately reproduce the experimentally known crystal structures of a small number of simple and well-characterized oxides, hydroxides, and oxyhydroxides, such as brucite, portlandite, quartz, kaolinite (Cygan *et al.*, 2004). In this approach, the individual atoms do not have their full formal charges, but rather carry so-called partial charges which empirically account for electron transfer in actual covalent bonds. Oxygen atoms, for instance, typically have partial charges of -0.8 to -1.1, rather than their formal value of -2.0. These partial atomic charges were derived from periodic density functional theory (DFT) quantum chemical calculations. Together with the VDW parameters, they were empirically optimized based on the experimental crystal structure refinements of the above model phases. The partial atomic charges also vary next to various cation substitution sites in the crystal structures. Thus, ClayFF empirically accounts for charge delocalization due to cation substitution in the clay structure (e.g., Al for Si, or Mg for Al) such that charge is partially shifted from the cationic center to neighboring oxygens depending on the local O-environment (Figure 2).

It is worth noting that very similar compositional and structural complications are also typical to other clay-related materials, such as layered double hydroxides (LDH), zeolites, various mineral phases of cement. Therefore, it is not surprising that ClayFF was almost immediately used in atomistic simulations of such phases as well (e.g., Kalinichev and Kirkpatrick, 2002; Kirkpatrick *et al.*, 2005b; Wang *et al.*, 2004,

2005a, 2006; Kalinichev *et al.*, 2007, 2014; Kumar *et al.*, 2007; Narasimhan *et al.*, 2009; Bushuev and Sastre, 2010; Kalinichev *et al.*, 2010; O'Brien *et al.*, 2016; Mutisya *et al.*, 2017; Androniuk *et al.*, 2017, 2020).

Thus, over the last 15 years, ClayFF has been successfully tested in numerous molecular simulations of a wide range of systems, showing good promise to further evolve into an adaptable and broadly effective force field for molecular simulations of clays, cement phases and other aluminosilicate materials and their interfaces with aqueous solutions. The following sections illustrate ClayFF application in atomistic simulations of several representative materials.

**Table 1.** “Non-bonded” parameters for the ClayFF force field (Cygan *et al.*, 2004).

Species	Symbol	Charge( $ e $ )	$D_o$ (kcal/mol)	$R_o$ (Å)
Water hydrogen	h*	0.4100	—	—
Hydroxyl hydrogen	ho	0.4250	—	—
Water oxygen	o*	-0.8200	0.1554	3.5532
Hydroxyl oxygen	oh	-0.9500	0.1554	3.5532
Bridging oxygen	ob	-1.0500	0.1554	3.5532
Bridging oxygen next to octahedral substitution	obos	-1.1808	0.1554	3.5532
Bridging oxygen next to tetrahedral substitution	obts	-1.1688	0.1554	3.5532
Bridging oxygen next to double substitution	obss	-1.2996	0.1554	3.5532
Hydroxyl oxygen next to substitution	ohs	-1.0808	0.1554	3.5532
Tetrahedral silicon	st	2.1000	$1.8405 \times 10^{-6}$	3.7064
Octahedral aluminum	ao	1.5750	$1.3298 \times 10^{-6}$	4.7943
Tetrahedral aluminum	at	1.5750	$1.3298 \times 10^{-6}$	3.7064
Octahedral magnesium	mgo	1.3600	$9.0298 \times 10^{-7}$	5.9090
Hydroxide magnesium	mgh	1.0500	$9.0298 \times 10^{-7}$	5.9090
Octahedral calcium	cao	1.3600	$5.0298 \times 10^{-6}$	6.2484
Hydroxide calcium	cah	1.0500	$5.0298 \times 10^{-6}$	6.2484
Octahedral iron	feo	1.5750	$9.0298 \times 10^{-7}$	5.5070
Octahedral lithium	lio	0.5250	$9.0298 \times 10^{-7}$	4.7257

## 4. Atomistic modeling of clay hydrous interlayers and interfaces

### 4.1. Hydration and swelling of clay minerals

For clay minerals and other similar materials capable of hydration and swelling, it is important to be able to assess quantitatively various thermodynamic characteristics of these processes.

The basal spacing as a function of water content essentially shows how the volume of the system changes with increasing (or decreasing) hydration. For an orthogonal simulation cell, from the results of  $NPT$ -ensemble MD simulation, the basal spacing ( $d$ ) can be calculated as follows:

$$d = \frac{\langle a \rangle \langle b \rangle \langle c \rangle}{2 \langle a \rangle \langle b \rangle} = \frac{\langle c \rangle}{2} \quad (18)$$

where  $\langle a \rangle$ ,  $\langle b \rangle$ , and  $\langle c \rangle$  are the statistically averaged dimensions of the simulation supercell (see Figure 1a).

The hydration energy ( $\Delta U$ ) can be used to evaluate the gain (or cost) of potential energy associated with water uptake by the dry clay, and can be calculated using the generic formula (e.g., Smith, 1998; Ngouana-Wakou and Kalinichev, 2014):

$$\Delta U = \frac{\langle U(N) \rangle - \langle U(0) \rangle}{N} \quad (19)$$

where  $N$  is the number of interlayer  $\text{H}_2\text{O}$  molecules for a given hydration level, while  $\langle U(N) \rangle$  and  $\langle U(0) \rangle$  are the average potential energies of the hydrated clay (with  $N$  water molecules), and dry clay ( $N = 0$ ), respectively.

The immersion energy ( $Q$ ) is the energy consumed or released when the clay system at a given hydration level is brought to another hydration level by adding water to the system (Smith, 1998):

$$Q = \langle U(N) \rangle - \langle U(N_0) \rangle - (N - N_0) U_{\text{bulk}} \quad (20)$$

where  $N_0$ , and  $\langle U(N_0) \rangle$  are the number of  $\text{H}_2\text{O}$  molecules and the average potential energy of a reference hydration level.  $U_{\text{bulk}}$  is the potential energy of bulk liquid water (per one  $\text{H}_2\text{O}$  molecule) under the same  $T$ - $P$  conditions in thermodynamic equilibrium with the clay.

Similarly, considering clay at a certain hydration level, the isosteric heat of water ad-

sorption can be calculated as a measure of energy released or consumed by the system when a small amount of water is added or removed from the system (Smith, 1998):

$$q_{\text{st}} = RT - \frac{\langle U(N) \rangle - \langle U(N') \rangle}{(N' - N)} \quad (21)$$

where  $N$ , and  $N'$  are two consecutive hydration levels,  $R$  is the ideal gas constant and  $T$  is the temperature. The factor of  $RT$  is needed for conversion between the internal energy and enthalpy.

Figure 3a illustrates the variation of basal layer spacing  $d$  in hydrated Cs-montmorillonite,  $\text{Cs}^+_{0.75}(\text{Si}_{7.75}\text{Al}_{0.25})(\text{Al}_{3.5}\text{Mg}_{0.5})\text{O}_{20}(\text{OH})_4 \cdot n\text{H}_2\text{O}$ , as a function of water content from the MD simulations with three models of montmorillonite that differ only by the degree of randomness in the distribution of octahedral and tetrahedral substitutions in their structure (Ngouana-Wakou and Kalinichev, 2014). The results for the three models, labelled *Uni*, *RanO*, and *RanTO*, are shown by filled circles with different degree of gray shading, while experimental data from several sources are shown by other symbols. No observable differences on the calculated layer spacing between the three clay models with different distribution of substitutions was observed. For all three clay models, a plateau corresponding to the formation of a stable monolayer hydrate is clearly observable at  $\sim 12.6$  Å, in good agreement with the range of 12.3 – 12.6 Å reported from experiments. In these simulations, the monolayer hydrate corresponds to  $n = 4.5$   $\text{H}_2\text{O}$  molecules per formula unit, which is in the range of 4.0 – 5.5 observed in other simulation studies (Ngouana-Wakou and Kalinichev, 2014).

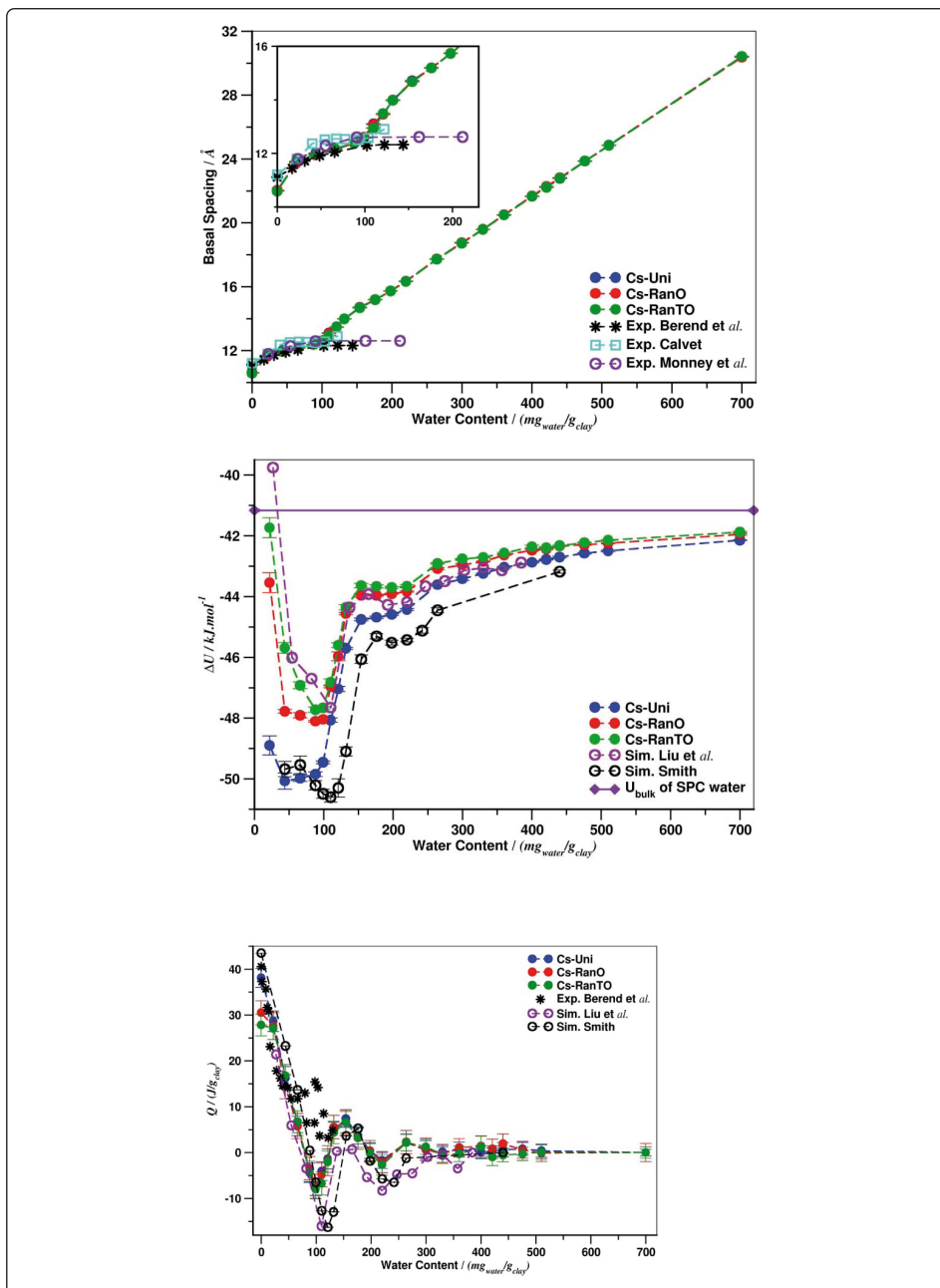


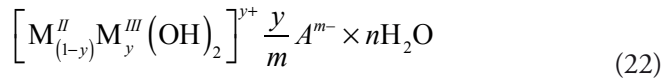
**Figure 3.** Top plot: Swelling curves of Cs-montmorillonite simulated with ClayFF (circles) compared with available experimental data (squares). The error bars for the simulated values, calculated with a 95% confidence interval, are within the size of the symbols. Middle and bottom plot show the hydration energy (Eq. 19) and immersion energy (Eq. 20) calculated from the same series of MD simulations (after Ngouana-Wakou and Kalinichev, 2014).

Beyond  $n = 4.5$  (or  $100 \text{ mg}_{\text{water}}/\text{g}_{\text{clay}}$  in Figure 3) experimental data indicate invariable layer spacings unlike the simulation swelling curves that increase. One has to remember, however, that the experimentally measured water contents include contributions not only from the  $\text{H}_2\text{O}$  molecules in clay interlayers, but also from the ones adsorbed on the external surfaces of clay particles and from the inter-particle pore-space, while the atomistic simulations using the periodic boundary conditions typically model infinite clay layers without any edges.

The hydration energies (Figure 3b) of the Cs-montmorillonite models are presented in Figure 3b together with the results of two other simulations (Smith, 1998; Liu *et al.*, 2008). All results exhibit two minima for water contents of  $n = 4.5$  ( $\sim 100 \text{ mg}_{\text{water}}/\text{g}_{\text{clay}}$ ) and  $n = 10.0$  ( $\sim 220 \text{ mg}_{\text{water}}/\text{g}_{\text{clay}}$ ). As expected, the hydration energies tend to approach the value of internal energy of bulk liquid water as the water content increases (horizontal solid line in Fig. 3b). The small differences between the results of three simulations can be attributed to the slightly different model structures used, but also to the different force fields employed in the simulations (see Ngouana-Wakou and Kalinichev (2014) for more details).

Further analysis of the swelling energetics based on the calculation of the immersion energy (Figure 3c) provides additional information for the clear identification of the water contents corresponding of the stable 1W and 2W hydration states. Apart from the completely dry state corresponding to the first points on the plots, the immersion energies calculated at all other water contents are very similar between the three clay models. Thus, Figure 3b allows us to better distinguish the previously observed monolayer and bilayer hydrates through the local minima for  $n = 4.5$  ( $\sim 100 \text{ mg}_{\text{water}}/\text{g}_{\text{clay}}$ ) and  $n = 10.0$  ( $\sim 220 \text{ mg}_{\text{water}}/\text{g}_{\text{clay}}$ ) for all simulation data presented.

Layered double hydroxides (LDHs), also known as anionic clays, represent another important class of swelling materials. Their lamellar structure is based on brucite-like  $\text{Mg}(\text{OH})_2$  layers and allows for a high degree of compositional variability via partial substitution of the divalent metal ions by trivalent metal ions leading to the permanent positive layer charge (e.g., Rives, 2001). The general chemical formula for many LDHs may be written as



where  $\text{M}^{\text{II}}$  and  $\text{M}^{\text{III}}$  are, respectively, the divalent and trivalent metal cations,  $y$  is the fraction of trivalent cations in the formula unit, and  $m$  is the charge of the anion. Typical  $\text{M}^{\text{II}}$  cations are  $\text{Mg}^{2+}$ ,  $\text{Ni}^{2+}$ ,  $\text{Fe}^{2+}$ ,  $\text{Mn}^{2+}$ , and  $\text{Zn}^{2+}$ , and typical  $\text{M}^{\text{III}}$  cations are  $\text{Al}^{3+}$ ,  $\text{Cr}^{3+}$ ,  $\text{Fe}^{3+}$  and  $\text{Co}^{3+}$ . The cations are octahedrally coordinated by the hydroxyl groups, forming two-dimensional sheets of edge-shared metal hydroxide octahedra. The charge balancing anions,  $\text{A}^{m-}$ , occur in the interlayer space and on particle sur-

faces, usually together with water molecules. The –O–H groups in the LDH structure are all oriented towards the interlayer or surface and can donate strong hydrogen bonds to the anions and H<sub>2</sub>O molecules. As in clays, the hydration state,  $n$  (water content per formula unit), can be broadly variable depending on many factors, such as the chemical nature of the anion ( $A^{m-}$ ), method of preparation, relative humidity, and the sample history (e.g., Rives, 2001).

Figure 4 shows the hydration energy of several Mg/Al-LDHs intercalated by various mono-, di-, and tri-valent organic anions simulated using the ClayFF force field (Kumar *et al.*, 2007; Kalinichev *et al.*, 2010). To make a relevant comparison between systems of various compositions, a uniform measure of the hydration state as the number of H<sub>2</sub>O molecules per number of structural hydroxide groups,  $x_{\text{H}_2\text{O}}$ , is used in Figure 4 independent of the formula unit, cationic/anionic composition, and charge of different LDHs. Unlike the montmorillonite swelling curves in Figure 3b, the computed hydration energies of Mg/Al-LDHs do not show a distinct minimum, but show instead the most negative values at low water contents, followed by relatively rapid change in the range  $0.2 < x_{\text{H}_2\text{O}} < 0.5$ , and slower, gradual approach to the potential energy for bulk liquid water for  $x_{\text{H}_2\text{O}} > 0.7$  (dashed horizontal line in Figure 4). However, these hydration energies are always noticeably lower in energy than that of the bulk liquid H<sub>2</sub>O (–44.1 kJ/mol for the SPC water model used) up to very high water contents, indicating the absence of specifically preferred hydration states for these LDHs and suggesting a tendency for the system to continuously adsorb water in water-rich environments, such as at high atmospheric relative humidity, and to eventually delaminate in aqueous suspensions. This is in distinct contrast with the swelling behavior and hydration energetics of similar LDHs intercalated by small inorganic anions, where experiments and atomistic simulations indicate the presence of restricted hydration ranges (Kirkpatrick *et al.*, 2005a, 2015).

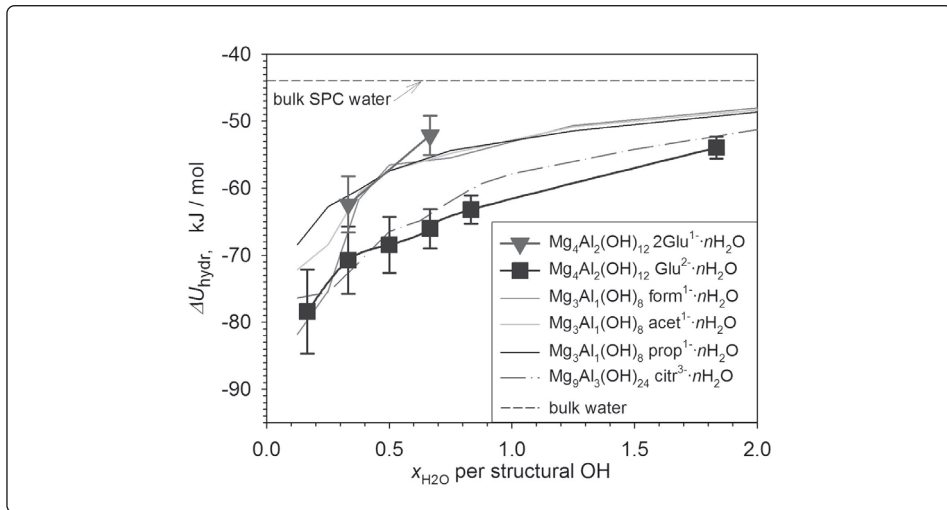


**Figure 4.** Hydration energy (Eq. 19) of Mg/Al-LDHs intercalated by mono- and di-valent glutamate anions as a function water content in the interlayer. Similar curves for Mg/Al-LDHs intercalated with other carboxylic acids (formate, acetate, propanoate, and citrate) are shown as thin lines without symbols for comparison (after Kalinichev *et al.*, 2010).

The swelling behavior of all the organo-intercalated Mg/Al-LDH phases in Figure 4 is largely due to the affinity of the carboxylic  $-\text{COO}^-$  groups for hydrogen bonds donated by  $\text{H}_2\text{O}$  molecules, which can better solvate them in a well integrated interlayer H-bonding network than the fixed  $-\text{OH}$  sites of the hydroxide layers. Compared to the LDHs intercalated with monocarboxylic anions (Kumar *et al.*, 2007), the superior swelling behavior (more negative hydration energies) of LDHs intercalated with higher-charge anions (like citrate $^{3-}$  or Glu $^{2-}$ ) is due to a combination of factors including greater incommensurability of the larger anions with the hydroxide layers, their ability to form stronger and more compact hydration shells due to their higher charge, and the resulting slower basal expansion under hydration. Taken together, these results show a stronger affinity for water for the Mg,Al-LDHs intercalated with higher-charge carboxylic anions. The trends for the monocarboxylic systems all approach the bulk water value at lower water contents than citrate $^{3-}$  or Glu $^{2-}$  LDHs.

#### 4.2 Structural properties of fluids and hydrogen bonding at clay-water interfaces

The structure of fluids is usually quantitatively analyzed in atomistic simulations via so-called atom-atom radial distribution functions,  $g_{ab}(r_{ab})$ , that represent a normalized average probability of finding an atom of type  $a$  at a certain distance  $r_{ab}$  from an atom of type  $b$  in the simulated system (Frenkel and Smit, 2002; Allen and Tildesley, 2017):

$$g_{\alpha\beta}(r_{\alpha\beta}) = \frac{\langle N_{\alpha\beta} \rangle}{4\pi\rho_{\beta}r_{\alpha\beta}^2} \quad (23)$$

where  $r_{\alpha\beta}$  is the distance between atoms  $\alpha$  and  $\beta$ ,  $\rho_{\beta}$  is the number density of atoms  $\beta$ , and  $\langle N_{\alpha\beta} \rangle$  the average number of atoms  $\beta$  found at the distance  $r_{\alpha\beta}$  from atom  $\alpha$ .

The number of neighbors, coordinating the selected atom at a certain distance (so-called running coordination number) can then be calculated as an integral of the radial distribution function:

$$n_{\alpha\beta}(r_{\alpha\beta}) = 4\pi\rho_{\beta} \int_0^{r_{\alpha\beta}} g(r)r^2 dr \quad (24)$$

In bulk liquid water, the oxygen-oxygen, oxygen-hydrogen, and hydrogen-hydrogen radial distribution functions look like in Figure 5a. This figure also provides a comparison of the simulated results with available experimental X-ray neutron diffraction data demonstrating a very good agreement. The most important features of these distributions (marked by a star symbol in Fig.5a) are the prominent first peak of the  $g_{\text{OH}}(r)$  function at  $\sim 1.9$  Å and the distinct maximum of the  $g_{\text{OO}}(r)$  function at  $\sim 4.5$  Å. Both of these features indicate strong local tetrahedral ordering of the neighboring  $\text{H}_2\text{O}$  molecules, with two molecules donating an H-bond ( $\sim 1.9$  Å long) to the selected molecule and two other molecules accepting similar H-bonds from the selected one. The H-bonds are indicated in Fig.5 as white dashed lines, while the edges of the tetrahedron ( $\sim 4.5$  Å long) are indicated by the black dashed lines (see, e.g., Kalinichev (2001, 2017) for further details).

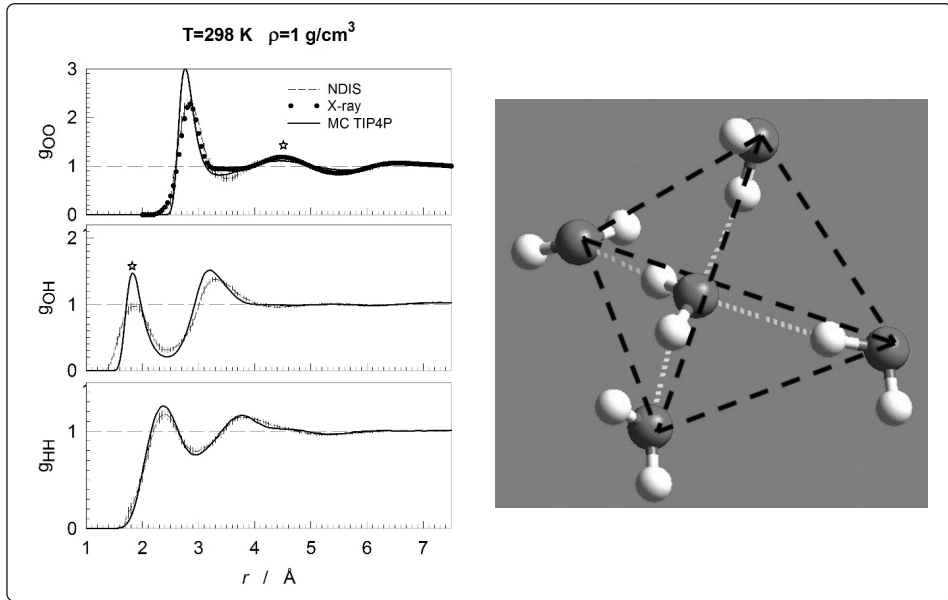


**Figure 5.** Atom-atom radial distribution functions of bulk liquid water illustrating the tetrahedral nearest-neighbor ordering of  $\text{H}_2\text{O}$  molecules due to hydrogen bonding.

For anisotropic systems, such as hydrated clay interlayers or interfaces (Figure 1), it is more informative to determine the fluid structure in terms of atomic density profiles of various solution species as function of their distance from the surface. Such functions can be calculated as the average number of atoms,  $\langle N_\alpha(z) \rangle$ , of certain type  $\alpha$  in solution at distance  $z$  from the surface, normalized by the system volume,  $V$ :

$$\rho_\alpha(z) = \frac{\langle N_\alpha(z) \rangle}{V} \quad (23)$$

where it is assumed that the coordinate axis  $z$  is perpendicular to the layering of our clay model, while the  $x$ - $y$  plane is parallel to the clay layering.

Another important quantitative structural characterization of the clay-solution interface can be obtained in the form of surface atomic density distributions of solution species. Such two-dimensional distributions in the  $x$ - $y$  plane within a layer of solution parallel to the surface are defined by the probability of finding an atom of type  $\alpha$  at a position  $(x, y)$  above the surface within a range of distances  $\Delta z$  close to the surface, typically corresponding to a mono-molecular layer of fluid ( $\sim 3$ - $5$  Å):

$$\rho_{\alpha, \Delta z}(x, y) = \frac{\langle N_{\alpha, \Delta z}(x, y) \rangle}{V} \quad (24)$$

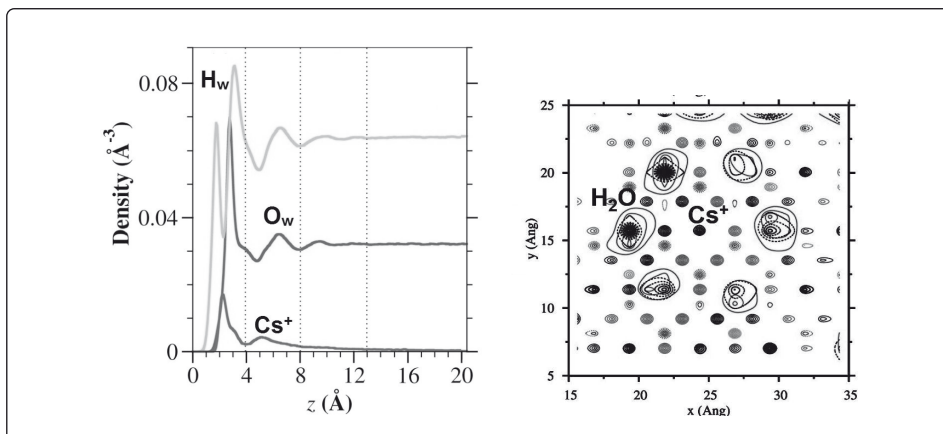


**Figure 6.** Atomic density profiles (left) and surface atomic density distributions (right) of  $Cs^+$  cations and  $H_2O$  molecules of the surface of Cs-montmorillonite. Dark dashed contours –  $O_w$ , light solid contours –  $H_w$ , light grey spots Si or Al of the siloxane surface of montmorillonite, dark grey spots – bridging oxygens,  $O_b$ , between Si- and Al- tetrahedra on the surface, to which surface  $H_2O$  molecules can donate one or two H-bonds (after Kalinichev *et al.*, 2017).

Such functions simulated for  $Cs^+$  ions in aqueous solution at the (001) surface of montmorillonite are shown in Figure 6. The time-averaged positions of the basal surface bridging oxygen atoms is taken here as a reference,  $z = 0$ .  $Cs^+$  ions are mostly adsorbed in the form of inner sphere complexes at distances  $\sim 2\text{--}3$   $\text{\AA}$  away from the montmorillonite surface (see Figure 6a). These  $Cs^+$  ions are located above the centers of di-trigonal cavities on the montmorillonite surface (Figure 6b). However, there is a visible atomic density of  $Cs^+$  at  $\sim 5\text{--}6$   $\text{\AA}$  indicating some amount of outer-sphere surface complexes. The position of the first adsorbed water peak  $O_w$  is correlated with the plane of surface adsorbed  $Cs^+$  ions clearly depicting that these  $H_2O$  molecules are strongly associated with the basal surface of muscovite and do not participate in the hydration of ions.

It should be noted that there are two possible predominant orientations of  $H_2O$  molecules at siloxane clay surfaces. They are schematically shown in Figure 7 as bidentate and monodentate orientations, respectively. In the bidentate configuration, the water molecule donates two weak H-bonds to the surface bridging oxygen atoms,  $O_b$  or  $O_{bts}$  in ClayFF (see Table 1), while in the monodentate orientation it can donate only one such bond.

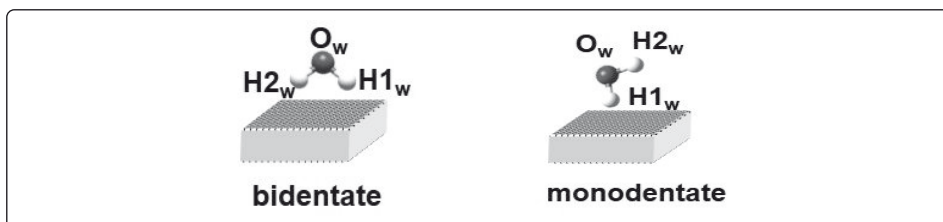


**Figure 7.** Schematic view of the predominant orientations of  $H_2O$  molecules on clay surfaces.

From the relative integral intensities of the peaks of  $O_w$  and  $H_w$  nearest to the surface in Figure 6, it is clear that most of the  $H_2O$  molecules are in monodentate orientation, and only a small fraction of water molecules correspond to the bidentate orientation. These are the ones that occupy the ditrigonal cavities next to the adsorbed  $Cs^+$  ions in Figure 6b.

The computed atomic density profiles also provide important insight into the ordering of  $H_2O$  molecules at hydroxylated surfaces, such as brucite, portlandite, or LDHs, but also many metal oxide surfaces that become easily hydroxylated at contact with water (e.g., Kalinichev and Kirpatrick, 2005; Machesky *et al.*, 2008; Kroutil *et al.*, 2020). On such a surface, two orientations of  $H_2O$  molecules are energetically most favorable for the formation of stable H-bonds. In one of them, water molecules have one H-atom directed toward an O-atom of the surface hydroxyl, thus donating a hydrogen bond to the surface. This configuration is similar to the monodentate orientation in Figure 7. However, on a hydroxylated surface,  $H_2O$  molecules can also accept H-bonds from the surface. Such accepting and donating  $H_2O$  orientations for three different surfaces are schematically shown at the top of Figure 8.

At the surface of portlandite (Figure 8a), the presence of a strong peak at  $\sim 1.8$  Å on the  $H_w$  density profile is due to the  $H_2O$  molecules donating H-bonds to the surface. In this orientation, the second H-atom of water molecules contributes to the peak at  $\sim 3.2$  Å. However, a stronger contribution to the 3.2 Å peak in the  $H_w$  distribution arises from the other favorable  $H_2O$  orientation, in which  $O_w$  atoms of  $H_2O$  molecules accept H-bonds donated by the surface hydroxyl groups. In this case, both hydrogens of the  $H_2O$  molecule contribute to the density profile peak at 3.2 Å. In both preferred orientations of  $H_2O$  molecules, the O-atoms are located approximately the same distance from the surface,  $\sim 3.0$  Å (Figure 8a). The ability of the surface  $H_2O$  molecules to both donate and accept H-bonds to the solid surface creates a very well developed H-bonding network across the interface with the structure strongly resembling that of bulk liquid water. Radial distribution functions  $g_{OO}$  and  $g_{OH}$  of liquid water are shown as dashed lines in Figure 8 to illustrate this similarity. Both signatures of tetrahedrally ordered H-bonding arrangements are clearly visible in the atomic density profiles (marked by stars in Figures 5 and 8). The interfacial water seems to be even slightly more structured than bulk water under the same thermodynamic conditions, and this ordering of the  $H_2O$  molecules is clearly visible even at distances up to 8 Å from the surface.

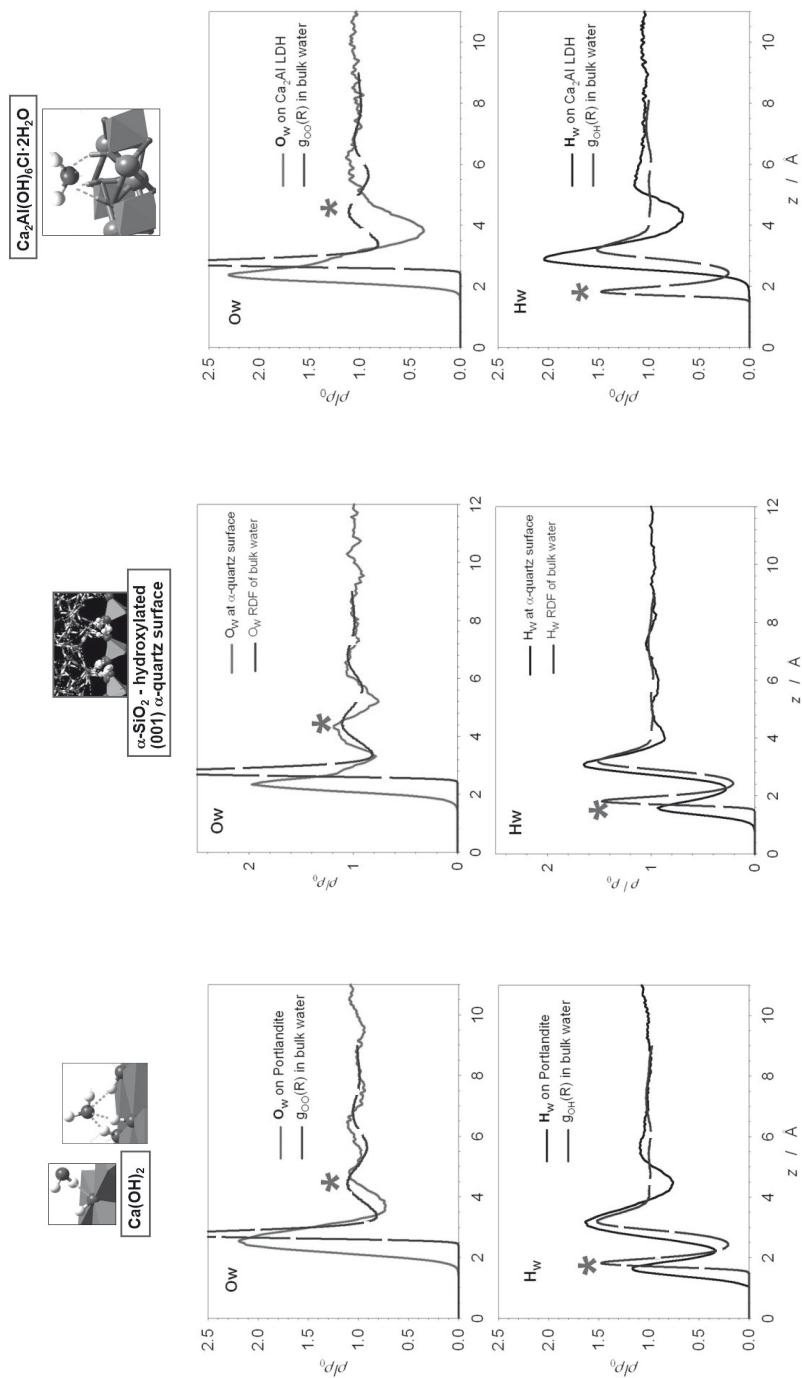


**Figure 8.** Atomic density profiles of interfacial  $\text{H}_2\text{O}$  molecules as functions of distance from the hydroxylated surfaces of portlandite (left), quartz (center), and  $\text{Ca}/\text{Al}$ -LDH (right). Dashed lines show the  $\text{O}^w\text{-O}^w$  and  $\text{H}^w\text{-O}^w$  radial distribution functions of bulk liquid water (Kalinichev, 2017) with stars marking the strong indicators of tetrahedral H-bonding molecular arrangements.

The situation is qualitatively similar for the hydroxylated aqueous interface of quartz (Kalinichev and Kirkpatrick, 2005) as illustrated by Figure 8b. However, for the Ca/Al-LDH (Figure 8c) the computed near-surface solution structure is strikingly different. Due to the positive structural charge of this phase and the predominance of direct coordination of the surface Ca sites by H<sub>2</sub>O molecules (Kalinichev *et al.*, 2000; Kalinichev and Kirkpatrick, 2002), the H-bond donation to the surface by water molecules becomes impossible, hence the well-interconnected H-bonding network is not formed in the interfacial region. This is clearly evident by the absence of both markers of tetrahedral nearest ordering of H<sub>2</sub>O molecules at the surface indicated by stars above the dashed lines in Figure 8c, representing  $g_{\text{OO}}$  and  $g_{\text{OH}}$  radial distribution functions of bulk liquid water.

### 4.3 Calculation of dynamic properties

Monte Carlo and molecular dynamics methods of atomistic computer simulations produce essentially equivalent results for the thermodynamic and structural properties of the modeled systems of interest. However, MD simulations have an advantage of providing also information about time-dependent dynamical phenomena and processes, such as molecular diffusion or the spectra of atomic motions.

The self-diffusion coefficients of the particles in the simulated system can be determined from their time-averaged mean squared displacement (MSD) according to the Einstein relation (Frenkel and Smit, 2002; Allen and Tildesley, 2017):

$$\frac{1}{N} \sum_{i=1}^N \left\langle \left| r_i(t) - r_i(t_0) \right|^2 \right\rangle = 2dDt \quad (25)$$

where  $N$  is the number of atoms of interest,  $r_i(t)$  is the position of atom  $i$  at time  $t$  and the angular brackets indicate the averaging taken over all time origins  $t_0$  along the MD trajectory.  $D$  in eq. (25) is the diffusion coefficient, and  $d$  is the dimensionality of the system, which is equal to 1, 2 or 3 for the calculation of one-dimensional, two-dimensional, or three-dimensional diffusion coefficients, respectively. For anisotropic systems, such as clay interlayers and interfaces, it can be very informative to separately calculate the diffusion coefficients in the direction within the layering,  $D_{xy}$ , and perpendicular to the layering,  $D_z$ , based on the respective projections of the atomic coordinates  $r_i$ .

This approach is widely used in the MD simulations of hydrated clays (e.g., Marry *et al.*, 2008, 2015; Churakov, 2013; Holmboe and Bourg, 2014; Ngouana-Wakou and Kalinichev, 2014) and related systems (e.g., Wang *et al.*, 2006; Kalinichev *et al.*, 2007; Korb *et al.*, 2007; Wu *et al.*, 2009).

MD-simulated dynamic trajectories of atoms can also be used to calculate so-called velocity autocorrelation functions (VACF) of specific atoms in the model system:

$$\text{VACF} \equiv C_{vv}(t) = \langle \mathbf{v}(0) \cdot \mathbf{v}(t) \rangle = \int \mathbf{v}(0) \cdot \mathbf{v}(t) d\Gamma \quad (26)$$

where the integration is performed over the entire *phase space* of the simulated system,  $G$  (e.g., McQuarrie, 2000).

Qualitatively, the VACF reflects a relative rate with which the system or its individual atoms lose “memory” of the velocities they had at a particular previous moment in time, indicated here as  $t = 0$ . Quantitatively, VACFs are calculated in MD simulations for each atomic type as:

$$C_{vv}(t) \equiv \langle \mathbf{v}(0) \cdot \mathbf{v}(t) \rangle = \frac{1}{N_t N} \sum_{i=1}^{N_t} \sum_{j=1}^N \mathbf{v}_j(t_i) \cdot \mathbf{v}_j(t_i + t) \quad (27)$$

where  $N_t$  is the number of time averages (using different independent time-origins as  $t = 0$ ),  $N$  is the number of atoms, and  $\mathbf{v}_j(t)$  the velocity of atom  $j$  at time  $t$  (Allen and Tildesley, 2017). The total system VACF is calculated over all atoms in the system, while the VACFs of individual atom types are calculated for all atoms of a given type.

Integration of VACF can be used as another way to determine atomic diffusion coefficients from MD simulations with the help of the Green-Kubo relation (Allen and Tildesley, 2017):

$$D = \lim_{t \rightarrow \infty} \frac{1}{3} \int_0^t \langle \mathbf{v}(0) \cdot \mathbf{v}(t') \rangle dt' \quad (28)$$

Another very useful application of VACFs is for the calculation of so-called power spectra of atomic motions (vibrational density of states) via the Fourier transformation (Allen and Tildesley, 2017):

$$P(\omega) = \int_0^\infty \frac{\langle \mathbf{v}(0) \cdot \mathbf{v}(t) \rangle}{\langle \mathbf{v}(0)^2 \rangle} \cos(\omega t) dt \quad (29)$$

$P(\omega)$  characterizes the dynamics of all atomic motions in the simulated system as a function of frequency. With certain restrictions, these power spectra can be compared to the experimental vibrational spectra of the same systems (e.g., Arab *et al.*, 2004; Kirkpatrick *et al.*, 2005a; Bougeard and Smirnov, 2007; Szczerba *et al.*, 2016a).

As with the diffusion coefficients, for anisotropic systems, such as clay interfaces and interlayers, it is also possible and very useful to calculate individual components of

the VACF tensor for a given atom type, and thus analyze the anisotropy of the motion. For layered materials, the three principal anisotropic contributions,  $XX$ ,  $YY$ , and  $ZZ$ , are very informative and provide quantitative insight into  $x$ -,  $y$ -, and  $z$ -projections of the vectors of atomic velocities and therefore the dynamics of atomic motions along different crystallographic directions. This, in turn, can greatly enhance vibrational band assignment and spectral interpretation. Usually, the  $x$ - and  $y$ -components of the atomic velocities are parallel to the layering, and the  $z$ -components are perpendicular to the layers. Thus, the  $XX$  and  $YY$  VACFs reflect the correlations of atomic motions within the plane parallel to the clay layers and the  $ZZ$  VACFs those perpendicular to the layers.

Figure 9 illustrates the application of this approach to the detailed quantitative understanding of the sharp high-frequency band of  $H_2O$  stretching vibrations of water molecules at the surface of montmorillonite (Szczerba *et al.*, 2016a). This sharp high-frequency IR band originating from adsorbed water is a common feature for all hydrated smectites (Kuligiewicz *et al.*, 2015). Its intensity does not depend much on the degree of clay hydration over a broad range of relative humidity, and its frequency has only a weak systematic decrease (red-shift) with increasing the total layer charge.

Thus, the sharp high-frequency IR band was attributed to a mechanism that must be common to all smectites at high hydration levels, regardless of interlayer cation.

In order to provide a quantitative explanation for the aforementioned experimental phenomenology, the power spectra for hydrogen atoms of the  $H_2O$  molecules on the clay surfaces were calculated for different smectites and compared to the spectrum of pure bulk liquid water simulated with the same molecular model (Szczerba *et al.*, 2016a).

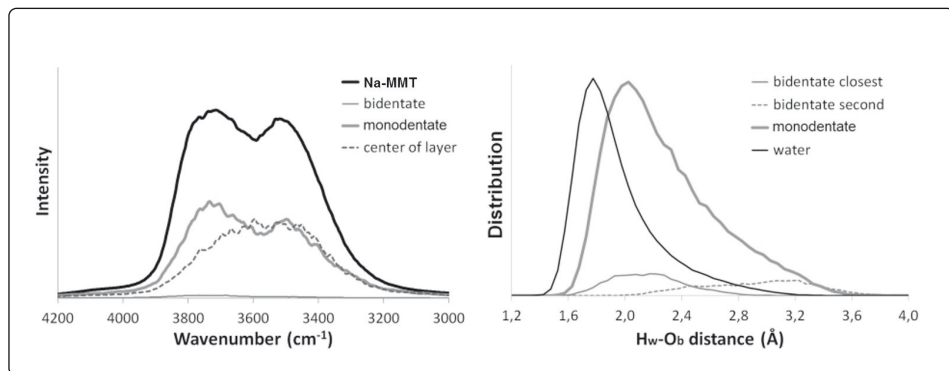


**Figure 9.** Left: power spectra of  $O_w-H_w$  stretching vibrations calculated for each individual sub-set of  $H_2O$  molecules on the surface of Na-montmorillonite: thin gray line – bidentate population, thick gray line – monodentate population, dashed line – water molecules away from the surface. Right: distributions of the shortest H-bonding distances of interfacial  $H_2O$  molecules with basal oxygens ( $O_w-H_w \cdots O_b$ ) in the bidentate and monodentate orientations, compared to distribution of  $O_w-H_w \cdots O_w$  distances in pure liquid water (after Szczerba *et al.*, 2016a).

For better quantitative understanding of the phenomenon, two distinct preferred surface-oriented types of H<sub>2</sub>O molecules (Figure 7) were identified in each simulation. Their atomic density profiles indicated that the predominantly bidentate-oriented molecules were located closer to the surface at  $z \sim 2.0$  Å (Figure 9b). A more strongly evident population of monodentate-oriented molecules population was located at somewhat larger distances of  $z \sim 2.8$  Å (Figure 9b). The presence of monodentate H<sub>2</sub>O was ubiquitous. This sub-population was abundantly visible for all smectites, all cations, and all hydration levels. The bidentate H<sub>2</sub>O population was far less abundant. It could be detected only in high charge smectites and was practically absent in their low charge analogs (Szczerba *et al.*, 2016a). Further growth of the amount of bidentate molecules can be predicted with layer charge increasing beyond  $1.0|e|$  per formula unit, which is consistent with its high contribution at charges approaching  $1.0|e|$  per formula unit, as observed in MD simulations of muscovite (Wang *et al.*, 2005b, 2009; Loganathan and Kalinichev, 2013; Teich-McGoldric *et al.*, 2014).

Calculations of the power spectra of specific sub-sets of interlayer and interfacial water hydrogen atoms were performed in order to explain in more detail which part of the surface H<sub>2</sub>O population is responsible for the sharp high-frequency vibrational band observed in the experimental spectra (Kuligiewicz *et al.*, 2015). Each sub-set of water molecules was defined by a common range of distances from the surface,  $z$ , and H<sub>2</sub>O dipole orientation angle,  $\alpha$ , with respect to the surface normal (Szczerba *et al.*, 2016a). An H<sub>2</sub>O molecule belongs to a certain sub-set if it is found within the same ( $z$ ,  $\alpha$ ) range in both the first and the last time-frame of the VACF calculation. In order to compare the contribution of each sub-set to the total spectrum, the spectral intensities calculated for montmorillonite are presented in Figure 9a are normalized to the number of H<sub>2</sub>O molecules identified in each sub-set (Szczerba *et al.*, 2016a).

This analysis demonstrated that the interfacial H<sub>2</sub>O molecules in bidentate and monodentate orientation with respect to the siloxane surface are both contributing to the experimentally observed sharp high-frequency O-H<sub>w</sub> stretching band of smectites (Kuligiewicz *et al.*, 2015). However, the number of H<sub>2</sub>O molecules in the monodentate orientation greatly exceeds that in the bidentate orientation and is, thus, the predominant contributor to the high-frequency vibrational band. In addition, it was possible to quantify that in the bidentate orientation each H<sub>2</sub>O molecule donates two H-bonds to the surface: one relatively strong, and another much weaker, while in the monodentate orientation it donates only one relatively weak H-bond to the surface. Increasing total clay layer charge results in increasing the number of bidentate-oriented H<sub>2</sub>O molecules, but also in decreasing the O<sub>w</sub>-H...O<sub>b</sub> distances for both monodentate-oriented and bidentate-oriented H<sub>2</sub>O populations. Both of these factors are eventually responsible for the red-shift of the sharp high-frequency band in smectites upon increasing the layer charge (Szczerba *et al.*, 2016a). The presence of the sharp high-frequency vibrational band in experimental and simulated

spectra can be considered as a strong evidence of intrinsic hydrophobicity of the siloxane surfaces of smectites, as has been recently demonstrated in another series of MD simulations (Szczerba *et al.*, 2020).

## 5. Atomistic modeling of other clay-related materials

Over the years, ClayFF has been also successfully applied to atomistic simulations of other nanoporous and nanostructured materials, such as zeolites (e.g., Narasimhan *et al.*, 2009; Bushuev and Sastre, 2010). Mishra *et al.* (2017) have recently provided a detailed comparison of various force fields for atomistic simulations of cementitious materials. Despite its simplicity, ClayFF is able to quite accurately reproduce the crystallographic parameters of many cement-related phases (Kalinichev and Kirkpatrick, 2002; Mutisya *et al.*, 2017).

However, in addition to structural properties, ClayFF has shown to reproduce the energetics of swelling for a wide range of cement-related silicates and hydroxides (e.g., Kalinichev *et al.*, 2007; Kirkpatrick *et al.*, 2015). Thus, the MD-simulated energetics of water sorption in Na- and K- kanemite,  $[(\text{Na},\text{K})\text{HSi}_2\text{O}_5 \cdot n\text{H}_2\text{O}]$ , is found in very good agreement with the observed X-ray diffraction, water sorption, TGA/DTA, and  $^{29}\text{Si}$  NMR data (Kirkpatrick *et al.*, 2005b). Kanemite-like local structures represent a significant component of gels produced during the so-called alkali-silica-reaction (ASR) in concrete that occurs primarily due to incorporation of  $\text{H}_2\text{O}$  molecules between kanemite-like nano-particles, rather than within their interlayer galleries (Kirkpatrick *et al.*, 2005b).

ClayFF is also shown to well reproduce ion and water sorption and diffusional dynamics at the surfaces of several typical cementitious materials, including hydrous calcium aluminates and the C-S-H phase represented by a tobermorite model (Kalinichev and Kirkpatrick, 2002; Korb *et al.*, 2007).

Androniuk *et al.* (2017) have recently developed a series of realistic ClayFF-based models of calcium silicate hydrates (the C-S-H phase is the principal component of cement) with different Ca/Si ratios and different degrees of surface protonation, using experimental NMR data and accurate quantum chemical results as a guidance. The models were then successfully applied to simulate adsorption of uranyl and gluconate ions at the hydrated C-S-H surfaces as a function of Ca/Si ratio and solution pH, and to interpret on the molecular scale the experimentally observed behavior of these systems (Androniuk *et al.*, 2017). The molecular level structural properties of the C-S-H interfaces were then investigated in classical MD simulations and local adsorption environments were identified for a range of Ca/Si ratios from 0.83 to 1.4. Several adsorption sites for uranyl cations on the C-S-H surfaces have been identified. Monodentate and bidentate complexes with respect to the surface can be

formed with deprotonated oxygens of the C-S-H phase. The same sites also adsorb  $\text{Ca}^{2+}$ , and a competition for these sites with the uranyl cations should be expected. Gluconate sorbs on the C-S-H phase by forming cation bridging inner-sphere and outer-sphere surface complexes (Androniuk *et al.*, 2017).

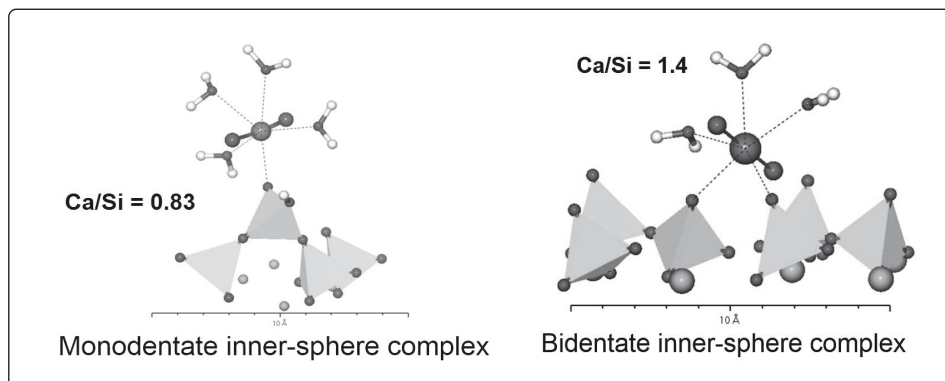


**Figure 10.** Typical coordination of hydrated inner-sphere surface complexes of uranyl,  $\text{UO}_2^{2+}$ , adsorbed at C-S-H surfaces with low (left) and high (right) Ca/Si ratios as simulated by Androniuk *et al.* (2017) using ClayFF. Grey tetrahedra – Si, small grey balls – Ca. 10-Å scale bar is shown below the structures.

In high-pH solutions typical of cement environment U(VI) exists in the form of uranyl cation  $\text{UO}_2^{2+}$  and is usually coordinated in the first hydration shell by 5  $\text{H}_2\text{O}$  molecules (some of which can be substituted by hydroxyl ions at high pH (Androniuk and Kalinichev, 2020)). The calculated atomic density profiles reveal clear differences in the uranyl/C-S-H interaction at two Ca/Si ratios (Figure 10). All adsorbed uranyl ions remain in the five-fold coordination with oxygens in the equatorial plane. Furthermore, the inner-sphere coordination of  $\text{UO}_2^{2+}$  appears to be the predominant type of interaction with the surface. There is also a preferential  $\text{UO}_2^{2+}$  coordination to the deprotonated sorption sites (more negatively charged). Therefore, when the surface silanol groups are all deprotonated under high pH conditions, the bidentate adsorption configuration is strongly predominant to the monodentate configuration.

## 6. Conclusions and Outlook

Atomistic computer simulation of materials using classical empirical force fields, such as ClayFF, has become over the last 15-20 years an indispensable powerful tool to study many nano-scale properties and processes in clay mineralogy and geochemistry. These methods of modeling are clearly complementary to many other well established experimental physical and chemical methods that are already widely used to characterize clay structure and study their properties. ClayFF has emerged as a

very simple but surprisingly successful force field for modeling clay-related phases, and especially the structure and dynamics of their aqueous interfaces and interlayers.

Present day atomistic computer simulations can qualitatively, and very often – even quantitatively, reproduce and predict the structure and properties clay minerals, their hydration and swelling properties, the structure and dynamics of their aqueous interfaces (Cygan *et al.*, 2009; Kalinichev *et al.*, 2016; Cygan and Myshakin, 2018). However, even if they are not competing with experimental methods in their accuracy, the most valuable feature of these techniques is their ability to greatly improve our physical understanding of the complex physical and chemical behavior of these systems and to unravel many important correlations between their structural, transport, spectroscopic, and thermodynamic properties on a fundamental atomic- and molecular-scale within a single consistent modeling approach that is based on a solid statistical-mechanical foundation. These methods are sometimes called “computer experiments”, but being neither pure theory, nor pure experiment, they can greatly stimulate the development of both theoretical and experimental studies of clay/water interfaces by providing necessary atomic-scale interpretation of sophisticated experimental data and thus leading to the construction of yet better models.

We already have a very high degree of quantitative molecular scale understanding of the interfacial phenomena on the basal (001) surfaces of clay minerals (Underwood *et al.*, 2016; Greathouse *et al.*, 2017; Willemsen *et al.*, 2019). The role of clay particle edges is also very important in many cases, but requires additional modeling efforts, which are also currently under way. In particular, a systematic work on improvement of the ClayFF parameterization is currently on-going along two directions important in view of their diverse range of applications: *i*) the development of additional metal-O-H bending terms (-Si-O-H, -Al-O-H, Mg-O-H, etc.) which facilitate the accurate description of the edges of clay particles (Pouvreau *et al.*, 2017, 2019) and lead to a more realistic simulations of finite size clay nanoparticles and their aggregates (e.g., Ho *et al.*, 2017, 2019; Lammers *et al.*, 2017); *ii*) making ClayFF fully compatible with more complex and accurate H<sub>2</sub>O molecular models in order to improve the accuracy of description of the structural and dynamic behavior of substrate-water interfaces and make it compatible with common force field for organic substances (e.g., Szcherba *et al.*, 2016a,b).

One principal limitation of ClayFF, as well as any other “non-reactive” classical force field, is that it does not allow to model ligand exchange reactions such as making and breaking of O-H bonds, thus preventing modeling of proton exchange reactions in the aqueous phase or on the surface, which can be important for many clay-related and especially cement-related systems. This limitation requires the researcher to make an a priori decision about the surface protonation state of the model to simulate, for instance, the pH dependent behavior. More rigorous approach would require the application of computationally very expensive *ab initio* MD techniques, or, at least,

application of a so-called “reactive” force field (e.g., Senftle *et al.*, 2016). The second approach, still being approximately 100 times more expensive computationally than a classical force field approach, is prone to its own uncertainties associated with empirical description of chemical reactivity. At the same time, classical approaches, such as ClayFF, being incapable to model the process of chemical reaction itself, can still be successfully applied to simulate the systems at various equilibrium states, e.g., before and after the reaction (e.g., Androniuk and Kalinichev, 2020).

Current challenges to a more realistic atomistic computational modeling of the adsorption and transport of fluids confined in clay-related materials include a better account of the true compositional and structural diversity and disorder of these materials, effects of interstratification, effects of organics in clay-organic interactions, the role of nanoparticle edges and multiscale phenomena of their aggregation. Many of these challenges can be addressed by simply using more powerful supercomputers to model larger and more disordered clay structures and longer simulation times with available force field parameterizations, such as ClayFF (e.g., Fernandez-Martinez *et al.*, 2020; Gonzalez *et al.*, 2020). New more powerful supercomputing facilities are becoming extremely helpful in allowing to address the observed phenomena at much larger geochemically and environmentally relevant time- and length- scales (e.g., Suter *et al.*, 2009; 2015), but closer collaboration between experimental and atomistic modeling approaches is necessary to make methods really successful.

## Acknowledgments

The paper was prepared with support of the industrial chair “Storage and Disposal of Radioactive Waste” at the Institut Mines-Télécom Atlantique, funded by ANDRA, Orano, and EDF. The financial support of the HSE University Basic Research Program is also gratefully acknowledged. Most of the calculations were performed using the supercomputing resources at CCIPL (Centre de Calcul Intensif des Pays de La Loire) and GENCI (Grand Équipement National de Calcul Intensif; projects A0020906921, A0040906921, A0060906921, and A0080906921).

## References

- Allen, M.P. and Tildesley, D.J. (2017) *Computer simulation of liquids*. 2nd edition. 626 p. Oxford University Press, New York.
- Androniuk, I. and Kalinichev, A.G. (2020) Molecular dynamics simulation of the interaction U(VI) with the c-s-h phase of cement in the presence of gluconate. *Applied Geochemistry*, **113**, 104496.
- Androniuk, I., Landesman, C., Henocq, P., and Kalinichev, A.G. (2017) Adsorption of gluconate and uranyl on C-S-H phases: Combination of wet chemistry experiments and molecular dynamics simulations for the binary systems. *Physics and Chemistry of the Earth, Parts A/B/C*, **99**, 194-203.

- Arab, M., Bougeard, D., and Smirnov, K.S. (2004) Structure and dynamics of interlayer species in a hydrated Zn-vermiculite. A molecular dynamics study. *Physical Chemistry Chemical Physics*, **6**, 2446-2453.
- Berendsen, H.J.C., Postma, J.P.M., van Gunsteren, W.F., and Hermans, J. (1981) Interaction models for water in relation to protein hydration. pp. 331-342 in *Intermolecular forces* (B. Pullman, editor), Riedel, Dordrecht, The Netherlands.
- Berendsen, H.J.C., Grigera, J.R., and Straatsma, T.P. (1987) The missing term in effective pair potentials. *Journal of Physical Chemistry*, **91**, 6269-6271.
- Bergaya, F., Theng, B.K.G., and Lagaly, G. (editors) (2006) *Handbook of Clay Science*. Elsevier Ltd.
- Botan, A., Marry, V., Rotenberg, B., Turq, P., and Noetinger, B. (2013) How electrostatics influences hydrodynamic boundary conditions: Poiseuille and electro-osmotic flows in clay nanopores. *Journal of Physical Chemistry C*, **117**, 978-985.
- Bougeard, D. and Smirnov, K.S. (2007) Modelling studies of water in crystalline nanoporous aluminosilicates. *Physical Chemistry Chemical Physics*, **9**, 226-245.
- Bushuev, Y.G., and Sastre, G. (2010) Atomistic simulations of water and organic templates occluded during the synthesis of zeolites. *Microporous and Mesoporous Materials*, **129**, 42-53.
- Churakov, S.V. (2013) Mobility of Na and Cs on montmorillonite surface under partially saturated conditions. *Environmental Science & Technology*, **47**, 9816-9823.
- Cygan, R.T. and Myshakin, E.M. (2018) Advances in molecular simulation studies of clay minerals. pp. 175-83 in *Greenhouse gases and clay minerals* (V. Romanov, editor), Springer.
- Cygan, R.T., Greathouse, J.A., Heinz, H., and Kalinichev, A.G. (2009) Molecular models and simulations of layered materials. *Journal of Materials Chemistry*, **19**, 2470-2481.
- Cygan, R.T., Liang, J.J., and Kalinichev, A.G. (2004) Molecular models of hydroxide, oxyhydroxide, and clay phases and the development of a general force field. *Journal of Physical Chemistry B*, **108**, 1255-1266.
- Delville, A. (1991) Modeling the clay water interface. *Langmuir*, **7**, 547-555.
- Fernandez-Martinez, A., Tao, J., Wallace, A.F., Bourg, I.C., Johnson, M.R., De Yoreo, J.J., Sposito, G., Cuello, G.J., and Charlet, L. (2020) Curvature-induced hydrophobicity at imogolite-water interfaces. *Environmental Science: Nano*, **7**, 2759-2772.
- Ferrage, E., Sakharov, B.A., Michot, L.J., Delville, A., Bauer, A., Lanson, B., Grangeon, S., Frapper, G., Jimenez-Ruiz, M., and Cuello, G.J. (2011) Hydration properties and interlayer organization of water and ions in synthetic Na-smectite with tetrahedral layer charge. Part 2. Toward a precise coupling between molecular simulations and diffraction data. *Journal of Physical Chemistry C*, **115**, 1867-1881.
- Frenkel, D., and Smit, B. (2002) *Understanding Molecular Simulation: From Algorithms to Applications*. 2nd edition. 638 p. Academic Press, San Diego.
- Gonzalez, R.I., Rojas-Nunez, J., Valencia, F.J., Munoz, F., Baltazar, S.E., Allende, S., Rogan, J., Valdivia, J.A., Kiwi, M., Ramirez, R., and Greathouse, J.A. (2020) Imogolite in water: Simulating the effects of nanotube curvature on structure and dynamics. *Applied Clay Science*, **191**, 105582.
- Greathouse, J.A., Durkin, J.S., Larentzos, J.P., and Cygan, R.T. (2009) Implementation of a Morse potential to model hydroxyl behavior in phyllosilicates. *Journal of Chemical Physics*, **130**, 134713-7.
- Greathouse, J.A., Cygan, R.T., Fredrich, J.T., and Jerauld, G.R. (2017) Adsorption of aqueous crude oil components on the basal surfaces of clay minerals: Molecular simulations including salinity and temperature effects. *Journal of Physical Chemistry C*, **121**, 22773-22786.

- Heinz, H., Lin, T.J., Mishra, R.K., and Emami, F.S. (2013) Thermodynamically consistent force fields for the assembly of inorganic, organic, and biological nanostructures: The INTERFACE force field. *Langmuir*, **29**, 1754–1765.
- Ho, T.A., Criscenti, L.J., and Greathouse, J.A. (2019) Revealing transition states during the hydration of clay minerals. *Journal of Physical Chemistry Letters*, **10**, 3704–3709.
- Ho, T.A., Greathouse, J.A., Wang, Y., and Criscenti, L.J. (2017) Atomistic structure of mineral nanoaggregates from simulated compaction and dewatering. *Scientific Reports*, **7**, 15286.
- Holmboe, M., and Bourg, I.C. (2014) Molecular dynamics simulations of water and sodium diffusion in smectite interlayer nanopores as a function of pore size and temperature. *Journal of Physical Chemistry C*, **118**, 1001–1013.
- Kalinichev, A.G. (2001) Molecular simulations of liquid and supercritical water: Thermodynamics, structure, and hydrogen bonding. *Reviews in Mineralogy & Geochemistry*, **42**, 83–129.
- Kalinichev, A.G. (2017) Universality of hydrogen bond distributions in liquid and supercritical water. *Journal of Molecular Liquids*, **241**, 1038–1043.
- Kalinichev, A.G. and Kirkpatrick, R.J. (2002) Molecular dynamics modeling of chloride binding to the surfaces of calcium hydroxide, hydrated calcium aluminate, and calcium silicate phases. *Chemistry of Materials*, **14**, 3539–3549.
- Kalinichev, A.G., and Kirkpatrick, R.J. (2005) Molecular dynamics simulation of the water/alpha-quartz interface. *Geochimica et Cosmochimica Acta*, **69**, A510–A510.
- Kalinichev, A.G., Kirkpatrick, R.J., and Cygan, R.T. (2000) Molecular modeling of the structure and dynamics of the interlayer and surface species of mixed-metal layered hydroxides: Chloride and water in hydrocalumite (Friedel's salt). *American Mineralogist*, **85**, 1046–1052.
- Kalinichev, A.G., Kumar, P.P., and Kirkpatrick, R.J. (2010) Molecular dynamics computer simulations of the effects of hydrogen bonding on the properties of layered double hydroxides intercalated with organic acids. *Philosophical Magazine*, **90**, 2475–2488.
- Kalinichev, A.G., Liu, X., and Cygan, R.T. (2016) Introduction to a special issue on molecular computer simulations of clays and clay-water interfaces: Recent progress, challenges, and opportunities. *Clays and Clay Minerals*, **64**, 335–336.
- Kalinichev, A.G., Loganathan, N., Ngouana-Wakou, B.F., and Chen, Z. (2017) Interaction of ions with hydrated clay surfaces: Computational molecular modeling for nuclear waste disposal applications. *Procedia Earth and Planetary Science*, **17**, 566–569.
- Kalinichev, A.G., Wang, J.W., and Kirkpatrick, R.J. (2007) Molecular dynamics modeling of the structure, dynamics and energetics of mineral-water interfaces: Application to cement materials. *Cement and Concrete Research*, **37**, 337–347.
- Kirkpatrick, R.J., Kalinichev, A.G., Wang, J., Hou, X., and Amonette, J.E. (2005a) Molecular modeling of the vibrational spectra of interlayer and surface species of layered double hydroxides. p. 239–285 in *The application of vibrational spectroscopy to clay minerals and layered double hydroxides* (J.T. Kloprogge, editor), *CMS Workshop Lecture Series*, **13**, The Clay Mineral Society, Aurora, CO.
- Kirkpatrick, R.J., Kalinichev, A.G., Hou, X., and Struble, L. (2005b) Experimental and molecular dynamics modeling studies of interlayer swelling: water incorporation in kanemite and ASR gel. *Materials and Structures*, **38**, 449–458.

Kirkpatrick, R.J., Kalinichev, A.G., Bowers, G.M., Yazaydin, A.Ö., Krishnan, M., Saharay, M., and Morrow, C.P. (2015) NMR and computational molecular modeling studies of mineral surfaces and interlayer galleries: A review. *American Mineralogist*, **100**, 1341-54.

Korb, J.P., McDonald, P.J., Monteilhet, L., Kalinichev, A.G., and Kirkpatrick, R.J. (2007) Comparison of proton field-cycling relaxometry and molecular dynamics simulations for proton-water surface dynamics in cement-based materials. *Cement and Concrete Research*, **37**, 348-350.

Kraevsky, S.V., Tournassat, C., Vayer, M., Warmont, F., Grangeon, S., Ngouana Wakou, B.F., and Kalinichev, A.G. (2020) Identification of montmorillonite particle edge orientations by atomic-force microscopy. *Applied Clay Science*, **186**, 105442.

Kroutil, O., Pezzotti, S., Gaigeot, M.-P., and Predota, M. (2020) Phase-sensitive vibrational SFG spectra from simple classical force field molecular dynamics simulations. *Journal of Physical Chemistry C*, **124**, 15253-15263.

Kuligiewicz, A., Derkowski, A., Szczerba, M., Gionis, V., and Chryssikos, G.D. (2015) Revisiting the infrared spectrum of the water-smectite interface. *Clays and Clay Minerals*, **63**, 15-29.

Kumar, P.P., Kalinichev, A.G., and Kirkpatrick, R.J. (2007) Molecular dynamics simulation of the energetics and structure of layered double hydroxides intercalated with carboxylic acids. *Journal of Physical Chemistry C*, **111**, 13517-13523.

Lammers, L.N., Bourg, I.C., Okumura, M., Kolluri, K., Sposito, G., and Machida, M. (2017) Molecular dynamics simulations of cesium adsorption on illite nanoparticles. *Journal of Colloid and Interface Science*, **490**, 608-620.

Liu, X.D., Lu, X.C., Wang, R.C., and Zhou, H.Q. (2008) Effects of layer-charge distribution on the thermodynamic and microscopic properties of Cs-smectite. *Geochimica et Cosmochimica Acta*, **72**, 1837-1847.

Loganathan, N. and Kalinichev, A.G. (2013) On the hydrogen bonding structure at the aqueous interface of ammonium-substituted mica: A molecular dynamics simulation. *Zeitschrift fur Naturforschung A*, **68**, 91-100.

Loganathan, N., Bowers, G.M., Yazaydin, A.O., Kalinichev, A.G., and Kirkpatrick, R.J. (2018) Competitive adsorption of H<sub>2</sub>O and CO<sub>2</sub> in 2-dimensional nano-confinement: GCMC simulations of Cs- and Ca-hectorite. *Journal of Physical Chemistry C*, **122**, 23460-23469.

Loganathan, N., Yazaydin, A.O., Bowers, G.M., Ngouana-Wakou, B.F., Kalinichev, A.G., and Kirkpatrick, R.J. (2020) Role of cations in the methane/carbon dioxide partitioning in nano- and mesopores of illite using constant reservoir composition molecular dynamics simulation. *Journal of Physical Chemistry C*, **124**, 2490-2500.

Machesky, M.L., Predota, M., Wesolowski, D.J., Vlcek, L., Cummings, P.T., Rosenqvist, J., Ridley, M.K., Kubicki, J.D., Bandura, A.V., Kumar, N., and Sofo, J.O. (2008) Surface protonation at the rutile (110) interface: Explicit incorporation of solvation structure within the refined MUSIC model framework. *Langmuir*, **24**, 12331-12339.

Marry, V., Rotenberg, B., and Turq, P. (2008) Structure and dynamics of water at a clay surface from molecular dynamics simulation. *Physical Chemistry Chemical Physics*, **10**, 4802-4813.

Marry, V. and Rotenberg, B. (2015) Upscaling strategies for modeling clay-rock properties. pp. 399-417 in *Developments in clay science* (C.Tournassat, C.I.Steefel, I.C.Bourg, and F.Bergaya, edsitors), v. 6, Elsevier.

McQuarrie, D.A. (2000) *Statistical Mechanics*. 641 p. University Science Books, Sausalito, CA.

- Mishra, R.K., Mohamed, A.K., Geissbühler, D., Manzano, H., Jamil, T., Shahsavari, R., Kalinichev, A.G., Galmarini, S., Tao, L., Heinz, H., Pellenq, R., van Duin, A.C.T., Parker, S.C., Flatt, R.J., and Bowen, P. (2017) Cemff: A force field database for cementitious materials including validations, applications and opportunities. *Cement and Concrete Research*, **102**, 68-89.
- Mutisya, S.M., de Almeida, J.M., and Miranda, C.R. (2017) Molecular simulations of cement based materials: A comparison between first principles and classical force field calculations. *Computational Materials Science*, **138**, 392-402.
- Narasimhan, L., Boulet, P., Kuchta, B., Schaefer, O., Denoyel, R., and Brunet, P. (2009) Molecular simulations of water and paracresol in MFI zeolite - A Monte Carlo study. *Langmuir*, **25**, 11598-11607.
- Ngouana-Wakou, B.F. and Kalinichev, A.G. (2014) Structural arrangements of isomorphous substitutions in smectites: Molecular simulation of the swelling properties, interlayer structure, and dynamics of hydrated Cs-montmorillonite revisited with new clay models. *Journal of Physical Chemistry C*, **118**, 12758-12773.
- O'Brien, C.J., Greathouse, J.A., and Tenney, C.M. (2016) Dissociation of sarin on a cement analogue surface: Effects of humidity and confined geometry. *Journal of Physical Chemistry C*, **120**, 28100-28109.
- Pouvreau, M., Greathouse, J.A., Cygan, R.T., and Kalinichev, A.G. (2017) Structure of hydrated gibbsite and brucite edge surfaces: DFT results and further development of the ClayFF classical force field with Metal-O-H angle bending terms. *Journal of Physical Chemistry C*, **121**, 14757-14771.
- Pouvreau, M., Greathouse, J.A., Cygan, R.T., and Kalinichev, A.G. (2019) Structure of hydrated kaolinite edge surfaces: DFT results and further development of the ClayFF classical force field with Metal-O-H angle bending terms. *Journal of Physical Chemistry C*, **123**, 11628-11638.
- Rives, V., Ed. (2001) *Layered Double Hydroxides: Present and Future*. 439 p. Nova Publishers.
- Sainz-Díaz, C.I., Hernández-Laguna, A., and Dove, M.T. (2001) Modeling of dioctahedral 2:1 phyllosilicates by means of transferable empirical potentials. *Physics and Chemistry of Minerals*, **28**, 130-41.
- Senftle, T.P., Hong, S., Islam, M.M., Kylasa, S.B., Zheng, Y., Shin, Y.K., Junkermeier, C., Engel-Herbert, R., Janik, M.J., Aktulga, H.M., Verstraelen, T., Grama, A., and van Duin, A.C.T. (2016) The ReaxFF reactive force-field: Development, applications and future directions. *Npj Computational Materials*, **2**, 15011.
- Skipper, N. T., Refson, K., and McConnell, J. D. C. (1991) Computer simulation of interlayer water in 2:1 clays. *Journal of Chemical Physics*, **94**, 7434-7445.
- Skipper, N.T., Chou Chang, F.-R., and Sposito, G. (1995a) Monte Carlo simulation of interlayer molecular structure in swelling clay minerals; 1, Methodology. *Clays and Clay Minerals*, **43**, 285-293.
- Skipper, N.T., Sposito, G., and Chou Chang, F.-R. (1995b) Monte Carlo simulation of interlayer molecular structure in swelling clay minerals. 2. Monolayer hydrates. *Clays and Clay Minerals*, **43**, 294-303.
- Smith, D.E. (1998) Molecular computer simulations of the swelling properties and interlayer structure of cesium montmorillonite. *Langmuir*, **14**, 5959-5967.
- Suter, J.L., Anderson, R.L., Greenwell, H.C., and Coveney, P.V. (2009) Recent advances in large-scale atomistic and coarse-grained molecular dynamics simulation of clay minerals. *Journal of Materials Chemistry*, **19**, 2482-2493.
- Suter, J. L., Groen, D., and Coveney, P. V. (2015) Chemically specific multiscale modeling of clay-polymer nanocomposites reveals intercalation dynamics, tactoid self-assembly and emergent materials properties. *Advanced Materials*, **27**, 966-984.

- Szczerba, M., Kuligiewicz, A., Derkowski, A., Gionis, V., Chryssikos, G.D., and Kalinichev, A.G. (2016a) Structure and dynamics of water-smectite interfaces: Hydrogen bonding and the origin of the sharp O-D<sub>w</sub>/O-H<sub>w</sub> infrared band from molecular simulations. *Clays and Clay Minerals*, **64**, 452-471.
- Szczerba, M. and Kalinichev, A.G. (2016b) Intercalation of ethylene glycol in smectites: Several molecular simulation models verified by X-ray diffraction data. *Clays and Clay Minerals*, **64**, 488-502.
- Szczerba, M., Kalinichev, A. G., and Kowalik, M. (2020) Intrinsic hydrophobicity of smectite basal surfaces quantitatively probed by molecular dynamics simulations. *Applied Clay Science*, **188**, 105497.
- Teich-McGoldrick, S.L., Greathouse, J.A., and Cygan, R.T. (2014) Molecular dynamics simulations of uranyl adsorption and structure on the basal surface of muscovite. *Molecular Simulation*, **40**, 610-617.
- Teleman, O., Jönsson, B., and Engström, S. (1987) A molecular dynamics simulation of a water model with intramolecular degrees of freedom. *Molecular Physics*, **60**, 193-203.
- Teppen, B.J., Rasmussen, K., Bertsch, P.M., Miller, D.M., and Schafer, L. (1997) Molecular dynamics modeling of clay minerals. 1. Gibbsite, kaolinite, pyrophyllite, and beidellite. *Journal of Physical Chemistry B*, **101**, 1579-1587.
- Tesson, S., Louisfremea, W., Salanne, M., Boutin, A., Ferrage, E., Rotenberg, B., and Marry, V. (2018) Classical polarizable force field to study hydrated charged clays and zeolites. *Journal of Physical Chemistry C*, **122**, 24690-24704.
- Underwood, T., Erastova, V., and Greenwell, H.C. (2016) Ion adsorption at clay-mineral surfaces: The Hofmeister series for hydrated smectite minerals. *Clays and Clay Minerals*, **64**, 472-487.
- Wang, J.W., Kalinichev, A.G., and Kirkpatrick, R.J. (2004) Molecular modeling of the 10-angstrom phase at subduction zone conditions. *Earth and Planetary Science Letters*, **222**, 517-527.
- Wang, J.W., Kalinichev, A.G., and Kirkpatrick, R.J. (2005a) Structure and decompression melting of a novel, high-pressure nanoconfined 2-d ice. *Journal of Physical Chemistry B*, **109**, 14308-14313.
- Wang, J.W., Kalinichev, A.G., Kirkpatrick, R.J., and Cygan, R.T. (2005b) Structure, energetics, and dynamics of water adsorbed on the muscovite (001) surface: A molecular dynamics simulation. *Journal of Physical Chemistry B*, **109**, 15893-15905.
- Wang, J.W., Kalinichev, A.G., and Kirkpatrick, R.J. (2006) Effects of substrate structure and composition on the structure, dynamics, and energetics of water at mineral surfaces: A molecular dynamics modeling study. *Geochimica et Cosmochimica Acta*, **70**, 562-582.
- Wang, J., Kalinichev, A.G., and Kirkpatrick, R.J. (2009) Asymmetric hydrogen bonding and orientational ordering of water at hydrophobic and hydrophilic surfaces: A comparison of water/vapor, water/talc, and water/mica interfaces. *Journal of Physical Chemistry C*, **113**, 11077-11085.
- Willemsen, J.A.R., Myneni, S.C.B., and Bourg, I.C. (2019) Molecular dynamics simulations of the adsorption of phthalate esters on smectite clay surfaces. *Journal of Physical Chemistry C*, **123**, 13624-13636.
- Wu, J.Y., Liu, Q.L., Xiong, Y., Zhu, A.M., and Chen, Y. (2009) Molecular simulation of water/alcohol mixtures: adsorption and diffusion in zeolite 4Å membranes. *Journal of Physical Chemistry B*, **113**, 4267-4274.
- Zeitler, T.R., Greathouse, J.A., Gale, J.D., and Cygan, R.T. (2014) Vibrational analysis of brucite surfaces and the development of an improved force field for molecular simulation of interfaces. *Journal of Physical Chemistry C*, **118**, 7946-7953.